

# A level set-based approach for modeling cellular rearrangements in tissue morphogenesis

Rhudaina Z. Mohammad<sup>a</sup>, Hideki Murakawa<sup>b</sup>, Karel Švadlenka<sup>a,c,1</sup>, Hideru Togashi<sup>d,e</sup>

<sup>a</sup>*Department of Mathematics, Graduate School of Science, Kyoto University, Kyoto, Japan*

<sup>b</sup>*Applied Mathematics and Informatics Course, Faculty of Advanced Science and Technology, Ryukoku University, Otsu, Japan*

<sup>c</sup>*Mathematical Institute, Czech Academy of Sciences, Prague, Czech Republic*

<sup>d</sup>*Department of Biochemistry and Molecular Biology, Kobe University Graduate School of Medicine, Kobe, Japan*

<sup>e</sup>*JST PRESTO (Precursory Research for Embryonic Science and Technology), Kobe, Japan*

---

## Abstract

Mathematical models and numerical simulations can provide an essential insight into the mechanisms through which local cell-cell interactions affect tissue-level cell morphology. Among such morphological phenomena, cellular patterns observed in developing sensory epithelia have gained keen attention of researchers in recent years, because they are thought to be of utmost importance for accurate sensory functions. However, most of current computational approaches to cellular rearrangements lack solid mathematical background and involve experimentally unreachable parameters, whereby only weak and ambiguous conclusions can be made based on simulation results. Here we present a simple mathematical model for tissue morphogenesis together with a level set-based numerical scheme for its solution as a tool to rigorously investigate evolving cellular patterns. This combined framework of a model and a numerical method features minimum possible number of physical parameters and guarantees reliability of simulation results, including correct handling of topology changes, such as cell intercalations. In this framework, we adopt the viewpoint of free energy minimization principle, and take cellular rearrangement as a gradient flow of a weighted surface energy associated with cell membrane, where the weights are related to physical parameters of the cells, for example, cell-cell adhesion and cell contractility. We present the applicability of this model to a wide range of tissue morphological phenomena, such as cell sorting, engulfment or internalization. In particular, we stress that this method is the first one to be successful in computationally reproducing the experimentally observed development of cellular mosaic patterns in sensory epithelia. Thanks to its simplicity and reliability, the model is able to capture the essence of biological phenomena, and may give a strong helping hand in deciphering unsolved questions of morphology.

*Keywords:* free energy minimization, cell intercalation, implicit cell morphology, localized auction dynamics, cellular pattern development

---

*Email addresses:* rhudaina@outlook.com (Rhudaina Z. Mohammad), murakawa@math.ryukoku.ac.jp (Hideki Murakawa), karel@math.kyoto-u.ac.jp (Karel Švadlenka), htogashi@med.kobe-u.ac.jp (Hideru Togashi)

<sup>1</sup>Corresponding Author

## 1. Introduction

Understanding the mechanisms of tissue morphogenesis – how interacting processes generate the shape and structure of an organism – is at the forefront of researches in developmental biology. In this paper, we focus on mathematical modeling as a tool to investigate how such local cell-cell interactions affect tissue-level morphology. As such, cell-cell junctions during epithelial tissue morphogenesis are constantly remodeled by mechanical forces. These individual (local) cell rearrangements trigger global tissue morphology when there is some form of highly-conserved force generation and transmission between cells, commonly realized by cadherin dependent cell-cell adhesion and cell cortical tension due to actin-myosin contraction (Heisenberg and Bellaïche, 2013; Dickinson et al., 2011). Within adherens junctions, the extracellular regions of cadherins form cis- and trans-homophilic clusters to adhere the cells to each other. By virtue of trans-interactions, cadherin complexes transmit tensile forces across actomyosin cortices of neighboring cells. Cadherin-catenin complexes are physically linked to the actomyosin cytoskeleton. The link between actomyosin and cadherin is thought to promote the regulation of cell adhesion by actomyosin contraction during cellular rearrangement in morphogenesis (Takeichi, 2014).

Cellular rearrangement is also regulated by differential adhesion at junctions. Previous studies indicated that nectins, a family of cell adhesion molecules, are implicated in the mosaic cellular pattern formation of various tissues (Togashi, 2016). Nectins and cadherins cooperatively regulate both cell-cell junction formation and cellular rearrangements. Cadherins prefer homophilic trans-interactions, but nectins prefer heterophilic trans-interactions to homophilic ones. When cells expressing different nectins were co-cultured, they arranged themselves into a mosaic pattern. This property of nectins contributes to the formation of a checkerboard pattern of the auditory epithelium and the mosaic pattern of the olfactory epithelium (Togashi and Katsunuma, 2017) (see also Figure 10 and 11). Live imaging analysis suggests that mosaic cellular patterning is the result of continuous intercalation of cells. These results were similar to those observed in the mixed culture of cells expressing different types of nectins, and supported the idea that differential adhesion between cells expressing different nectins drives cell intercalations.

Intercalation processes require a distinctive combination of mechanisms, including adhesive changes that allow cells to rearrange, or cytoskeletal events through which cells exert the forces needed for cell neighbor exchange. Differential adhesiveness at each junction might contribute to the shrinkage and extension of the junction. These junctional regulation mechanisms might mutually affect cell cortical tension through actin-myosin and their mechanics. However, the relation between differential adhesion and cortical tension during cellular rearrangement in morphogenesis and cell sorting processes is still unclear.

To analyze the effect of these and other factors in tissue self-organization, a number of mathematical models have been proposed with the assumption that tissue evolves via a succession of quasi-equilibrium states, that is, cell shapes are described by their instantaneous state of lowest energy (Steinberg, 1963). In this article, we follow this line and focus on a class of models which neglect inertial effects and treat the evolution of a cellular aggregate from the viewpoint of free energy minimization principle. In particular, we

37 look at models where surface free energy, i.e., energy associated with cell membrane, is important. To be more  
 38 precise, we consider cellular rearrangement as the  $L^2$ -gradient flow of a weighted surface energy constrained  
 39 by the condition that each cell preserves its volume to a certain extent. We remark that continuum models  
 40 have been developed that successfully reproduce cellular patterns formed due to cell-cell adhesion and other  
 41 factors (Armstrong et al., 2006; Carrillo et al., 2019). Such models do not take into account the shape of  
 42 each individual cell and deal with morphogenetic phenomena on the macroscopic level of cell populations.  
 43 Meanwhile, in this paper our objective is to understand the mechanisms of interactions among cells on the  
 44 microscopic level, and thus we need to precisely resolve the shape of each cell.

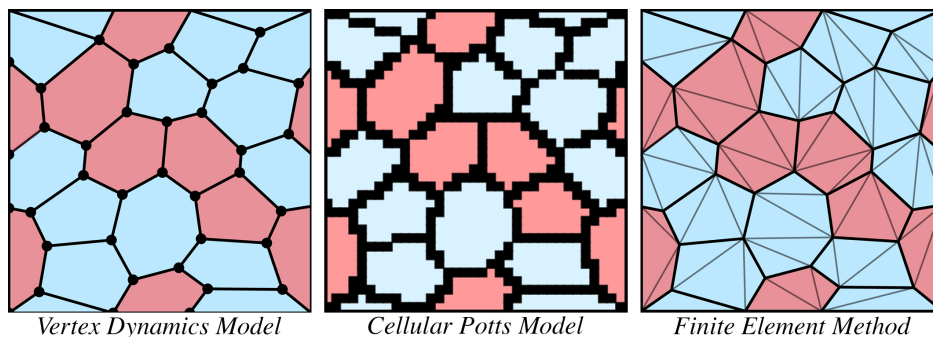


Figure 1: Existing mathematical models for tissue morphogenesis. An aggregate of red and blue cells geometrically represented according to vertex dynamics model, cellular Potts model, and finite element method.

45 Existing computational models based on this type of free energy minimization include, among others,  
 46 vertex dynamics model, cellular Potts model, and finite element methods. The main difference of these  
 47 approaches lies in how cells are geometrically represented (see Figure 1). Vertex dynamics model (Honda,  
 48 1983; Nagai and Honda, 2001; Honda et al., 2004; Fletcher et al., 2013) represents cells as polygons where  
 49 mechanical forces are applied to its vertices. In this model, polygonal vertices migrate so as to decrease  
 50 an energy potential, which includes a penalty term to enforce each cell's preferred volume. Such geometric  
 51 representation, however, cannot precisely approximate cell-cell junctions of complex shapes with nonzero  
 52 curvature and tissues composed of cells with significantly differing sizes. Typical examples of such complex  
 53 tissues are the auditory (Togashi et al., 2011) and olfactory epithelium (Katsunuma et al., 2016). We apply  
 54 our method to such tissues in Section 6 (see Figure 10). Cellular Potts model (Graner and Glazier, 1992;  
 55 Glazier and Graner, 1993), on the other hand, discretizes the continuous cell aggregate configuration onto  
 56 a fixed regular lattice; thereby, representing each cell as a number of grid points. At each grid point, one  
 57 calculates how the energy (based on cell-cell adhesion, cell incompressibility, and chemotaxis) changes as the  
 58 grid point transitions to a randomly selected neighbor. If this elicits a decrease in energy, the grid point is  
 59 allowed to transition to its neighbor. As a result, when a cell moves, it may lose or gain some grid points  
 60 on the lattice. In this model, cell contact angles are restricted to discrete values determined by the choice  
 61 of the lattice, and thus cannot be well approximated. Lastly, finite element method (Brodland and Gordon,  
 62 1994; Chen and Brodland, 2000; Brodland and Veldhuis, 2002) partitions polygonal cells into a finite number

63 of elements to solve mechanical equations characterizing tissue dynamics. In the two-dimensional setting,  
64 each cell-cell junction is represented as a piecewise linear curve and interfacial tensions are modeled using  
65 constant force on point masses along each cell-cell junction. In this sense, this formulation acts like the  
66 vertex dynamics model.

67 Although each specific morphogenetic phenomenon involves a large number of biological and physical  
68 factors, it is a well accepted understanding in the modeling community that it is not reasonable to con-  
69 struct models having a large number of factors as model parameters. The reason is simply the fact that  
70 correlation analysis becomes prohibitively complicated with increasing number of parameters, especially in  
71 living systems: if a model has a sufficiently large number of parameters, their suitable tuning can produce  
72 essentially arbitrary results and the analysis becomes pointless. This leads researchers to pin down biolog-  
73 ically significant factors in a given phenomenon, and build a model with only those factors as parameters.  
74 However, the aforementioned models incorporate a number of parameters which cannot be omitted and have  
75 only vague physical interpretations. For example, to deal with necessary topological changes due to cellu-  
76 lar intercalations while keeping proper vertex connectivity, one performs junctional rearrangements in the  
77 vertex dynamics model through simple operations, e.g., T1 (cell neighbor exchange), T2 (cell removal due  
78 to shrinkage), and T3 (vertex/edge merging) transitions (Fletcher et al., 2013); and in the finite element-  
79 based method through a boundary "flip" algorithm (Brodland, 2004) (equivalent to T1 transition), which  
80 all require additional parameters.

81 To overcome the disadvantages of existing methods, we present a general mathematical model together  
82 with an accurate and effective level set-based method of its numerical solution, which enjoys four significant  
83 benefits: (1) it is able to express arbitrary shapes of cellular junctions, in particular, curved ones; (2) it can  
84 reproduce the correct cell contact angles; (3) it has the minimal possible number of parameters with the  
85 option of adding new parameters according to necessity; and (4) it can naturally handle topology changes  
86 without relying on artificial procedures that inevitably involve unphysical parameters. Hence, the presented  
87 model is well suited for testing various hypotheses related to developmental morphology. We support this  
88 fact in Section 6 using the example of formation of cellular patterns in sensory epithelia. As mentioned  
89 above, such pattern formation entails complex curved shapes of cell junctions, largely different cell sizes and  
90 frequent topology changes, which make its numerical simulation challenging.

## 91 **2. Level Set-Based Approach**

92 Let us now present the mathematical model and the numerical algorithm for its solution.

93 We start with the formulation of the mathematical model. We represent an aggregate of cells as a  
94 bounded domain  $\Omega \subset \mathbb{R}^d$  ( $d = 2$  or  $3$ ) partitioned into  $N$  closed sets  $\mathcal{C}_1, \dots, \mathcal{C}_N$ , representing *cells* (see  
95 Figure 2 for the basic notation). It naturally follows that *cell-cell junction*  $\gamma_{ij} := \mathcal{C}_i \cap \mathcal{C}_j = \partial\mathcal{C}_i \cap \partial\mathcal{C}_j$  is the  
96 boundary between cells  $\mathcal{C}_i$  and  $\mathcal{C}_j$ . We consider cellular rearrangement as the  $L^2$ -gradient flow (see (Laux

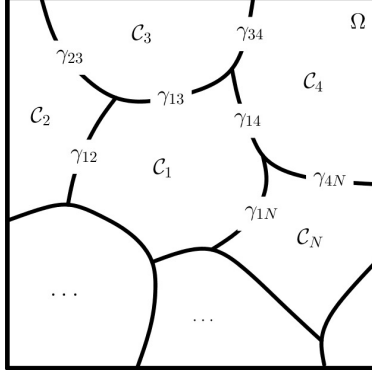


Figure 2: Setup and basic notation of the model. A cellular aggregate is represented as a bounded domain  $\Omega$  partitioned into  $N$  cells:  $\mathcal{C}_1, \dots, \mathcal{C}_N$  as closed sets. Moreover, the boundary between cells  $\mathcal{C}_i$  and  $\mathcal{C}_j$  denotes the cell-cell junction  $\gamma_{ij}$ .

97 and Otto, 2016) and references therein for a precise definition) of the weighted surface energy

$$E(\mathcal{C}_1, \dots, \mathcal{C}_N) = \sum_{i \neq j} \sigma_{ij} \text{Area}(\gamma_{ij}) \quad (1)$$

98 constrained by each cell's prescribed volume  $V_\ell^0$  ( $\ell = 1, 2, \dots, N$ ). Here, the weights  $\sigma_{ij} = \sigma_{ji} > 0$  for  
 99  $i \neq j$  may be related to cell-cell adhesion and/or cell contractility (see Section 3 for more). When  $i = j$ , we  
 100 formally set  $\sigma_{ij} = \sigma_{ii} = 0$ .

101 In materials science, this problem (considered without volume constraint to begin with) is widely known  
 102 as the Mullins (1999) model for normal grain growth where  $\mathcal{C}_i$  denotes a crystallite/grain in polycrystalline  
 103 materials. To realize the least energy, lower semicontinuity of the functional is required, a necessary and  
 104 sufficient condition for which is the triangle inequality  $\sigma_{ik} \leq \sigma_{ij} + \sigma_{jk}$  for any distinct  $i, j$  and  $k$  (Morgan,  
 105 1997). The grain boundary  $\gamma_{ij}$  in the  $L^2$ -gradient flow moves with a velocity  $\mu_{ij} \sigma_{ij} \kappa_{ij} \boldsymbol{\eta}_{ij}$  where  $\kappa_{ij}$ ,  $\mu_{ij}$  and  
 106  $\boldsymbol{\eta}_{ij}$  denote the mean curvature, mobility, and unit normal of  $\gamma_{ij}$ , respectively. Moreover, at the junction where  
 107 three grains  $\mathcal{C}_i$ ,  $\mathcal{C}_j$ , and  $\mathcal{C}_k$  meet, the Herring (1999) angle condition holds, that is,  $\sigma_{ij} \boldsymbol{\eta}_{ij} + \sigma_{jk} \boldsymbol{\eta}_{jk} + \sigma_{ik} \boldsymbol{\eta}_{ik} = 0$ .  
 108 Thus, grain boundaries in the annealing of pure metals (with equal surface tensions) evolve by mean curvature  
 109 flow, where triple junctions meet at angles of  $120^\circ$ .

110 Although the mathematical model is simple, its numerical realization is not at all obvious. The rest  
 111 of this section is devoted to the explanation of the background of the numerical scheme that we propose.  
 112 Earlier works in simulating the above mentioned grain boundary motion involve front tracking (Bronsard  
 113 and Wetton, 1995), which discretizes grain boundaries into finite number of points at which the mean curva-  
 114 ture is explicitly calculated to determine its position at next time step. This resembles the vertex dynamics  
 115 model, in the sense that both approaches evolve vertices based on explicitly calculated quantities. Conse-  
 116 quently, its major drawback lies in its inability to handle grain boundaries that cross or have complicated  
 117 topologies. Proper approximation of the subsequent evolution then requires some form of ad hoc “numerical  
 118 surgery”, which may lack physical justification and can be impractical to implement, particularly in three

119 dimensions. To alleviate this drawback, Merriman et al. (1994) introduced the MBO thresholding scheme  
 120 for diffusion-generated curvature-dependent motion of multiple junctions, which is based on the level set for-  
 121 mulation of Osher and Sethian (1988) for propagating fronts with curvature-dependent speed. This scheme  
 122 tracks interfaces implicitly by following level sets – allowing it to naturally handle topological changes. In  
 123 recent years, Esedoğlu and Otto (2015) extended the MBO method to realize motion of grain boundaries in  
 124 polycrystalline materials with arbitrary surface tensions. This method inherits the main advantages of the  
 125 MBO approach: efficiency in the sense of low computational cost; and under a mild condition on the weights  
 126  $\sigma_{ij}$ , gradient stability in the sense that in every time step the energy (1) is decreased.

127 With the aforementioned advantages, we introduce a level set-based numerical algorithm to simulate cell  
 128 dynamics in tissue morphogenesis. It is based on the Esedoğlu-Otto algorithm but incorporates cell volume  
 129 constraints and other aspects typical for cells. Incorporating volume constraints in the energy approximation  
 130 technique of Esedoğlu and Otto (2015) leads to the following optimization strategy: we describe a given  $N$ -  
 131 cell configuration at discrete time  $t_k$  by the level set vector field  $\mathbf{u}^k := (u_1^k, \dots, u_N^k) : \Omega \rightarrow [0, 1]^N$ , and obtain  
 132 the configuration  $\mathbf{u}^{k+1}$  at the next time step  $t_k + \delta t$  by minimizing a linear functional:

$$\mathbf{u}^{k+1} = \arg \min_{\mathbf{u} \in \mathcal{K}} \frac{2}{\sqrt{\delta t}} \sum_{i=1}^N \int_{\Omega} u_i \varphi_i^k, \quad \text{where} \quad \varphi_i^k := \sum_{j=1}^N \sigma_{ij} G_{\delta t} * u_j^k, \quad (2)$$

and  $G_{\delta t}$  is the Gaussian kernel, over the convex constraint set

$$\mathcal{K} := \left\{ \mathbf{u} \in [0, 1]^N : \sum_{j=1}^N u_j(x) = 1, \text{ a.e. } x \in \Omega \text{ and } \int_{\Omega} u_j = V_j^0, j = 1, \dots, N \right\},$$

133 (see Appendix A for a more detailed explanation). Without the volume requirement in the constraint set  $\mathcal{K}$ ,  
 134 this reduces to the original Esedoğlu-Otto scheme.

135 To numerically implement (2), a straightforward scheme is to incorporate volume constraints with La-  
 136 grange multipliers, however, a more efficient approach employs auction algorithms (Jacobs et al., 2018).  
 137 The idea is to assign cell membership to each point of the discretized domain  $\Omega_m = \{x_1, \dots, x_m\} \subset \Omega$  by  
 138 simulating an auction, so that each cell  $\mathcal{C}_j$  contains  $v_j$  points, where the integers  $v_j$  are chosen in such a way  
 139 that the mass ratios  $v_j / \sum_k v_k$  are as close to  $V_j^0 / |\Omega|$  as possible.

140 The Esedoğlu-Otto scheme is simple and efficient but there are some issues that need to be tackled,  
 141 in particular, the phenomena of wetting and nucleation (Esedoğlu and Otto, 2015). Failure to satisfy the  
 142  $\sigma$ -triangle inequality condition leads to wetting, where a new cell  $\mathcal{C}_k$  suddenly appears along the cell-cell  
 143 junction  $\gamma_{ij}$ . Moreover, even when  $\sigma$ -triangle inequality is satisfied, a new cell may still get nucleated at a  
 144 tricellular junction. For evolutions computed with auction dynamics, due to preservation of cell volumes,  
 145 such wetting and nucleation will force a cell to split into two or more disjoint parts, some of which transfer  
 146 to the wetting or nucleation regions. It is important to address this issue since such cell splitting phenomena  
 147 do not occur during cellular rearrangements; yet it is possible that  $\sigma_{ij}$ 's may not necessarily satisfy the  
 148 triangle inequality condition in real tissues. To this end, we modify the auction algorithm by incorporating a

149 topological constraint, so as to preserve cell connectivity. This makes sense physically, since individual cells  
 150 only move in response to their local surroundings, i.e., to their neighboring cells. Hence, when we estab-  
 151 lish cell membership, we only allow local bidding processes in the auction, as shown in the following algorithm.

152

153 **Algorithm** (for numerical approximation of the  $L^2$ -gradient flow of the energy (1) with preservation of  
 154 cell volumes and connectivity)

155 **Notation:**  $\chi_C$  denotes the characteristic function of a set  $C$ ; and  $G_{\delta t}(x) = (4\pi\delta t)^{-\frac{d}{2}} e^{-\frac{|x|^2}{4\delta t}}$  is the  $d$ -  
 156 dimensional Gaussian kernel.

157 **Initialization:** Split the time interval  $[0, T]$  into  $K$  subintervals of equal length  $\delta t = T/K$ , and set  
 158 discrete time levels  $t_k = k\delta t$ ,  $k = 1, \dots, K$ . Discretize the computational domain  $\Omega$  into a finite grid  
 159  $\Omega_m = \{x_1, \dots, x_m\}$ , and assign each discrete point  $x \in \Omega_m$  to a cell region  $C_j$  defining thus the initial  
 160 discrete aggregate of cells  $C_1^0, \dots, C_N^0$ . For each  $j = 1, \dots, N$ , record the number  $v_j$  of grid points in  $C_j$ .

161 **Input:** Discrete cell aggregate  $C_1^k, \dots, C_N^k$  and weights  $\{\sigma_{ij}^k\}_{i,j=1}^N$  at time  $t_k$ ; parameter  $0 < \varepsilon \ll 1$  for the  
 162 auction algorithm.

163 **Output:** Discrete cell aggregate  $C_1^{k+1}, \dots, C_N^{k+1}$  at next time  $t_{k+1} = t_k + \delta t$ .

164 1. *Convolution.* For each  $x \in \Omega_m$ , compute

$$\psi_i^k(x) := 1 - \sum_{j=1}^N \sigma_{ij}^k G_{\delta t} * \chi_{C_j^k}(x). \quad (3)$$

165 2. *Localized Auction Dynamics.* For all  $j = 1, \dots, N$ , initialize  $p_j = 0$  and  $C_j^{k+1} = \emptyset$ . For each unassigned  
 166  $x \in \Omega_m$ , do

167 (a) Find the set of neighboring cells of the cell  $C_i^k$  to which  $x$  was previously assigned:  $\mathcal{N}_x := \{j :$   
 168  $\partial C_i^k \cap \partial C_j^k \neq \emptyset\}$ .

169 (b) Determine

$$i^* = \operatorname{argmax}_{i \in \mathcal{N}_x} (\psi_i^k(x) - p_i), \quad i^\# = \operatorname{argmax}_{i \in \mathcal{N}_x \setminus \{i^*\}} (\psi_i^k(x) - p_i) \quad (4)$$

170 (c) Calculate the bid  $b(x) = p_{i^*} + \varepsilon + (\psi_{i^*}^k(x) - p_{i^*}) - (\psi_{i^\#}^k(x) - p_{i^\#})$ .

171 (d) If  $|\mathcal{C}_{i^*}^{k+1}| < v_{i^*}$ , assign  $x$  to  $C_{i^*}^{k+1}$ . Otherwise, replace the point in  $C_{i^*}^{k+1}$  with the lowest bid by  $x$ .

172 (e) Update the price  $p_{i^*} = \min_{z \in C_{i^*}^{k+1}} b(z)$ .

173 We now briefly comment on the parameters related to the numerical implementation. The discretization  
 174 parameters are the number  $m$  of discrete points in the computational domain  $\Omega$  and the time step  $\delta t$ . The  
 175 convolutions (3) in each step are efficiently computed on rectangular grids using fast Fourier transform (FFT)  
 176 algorithm with a complexity of  $O(m \log m)$  operations. The time step can be adaptively changed throughout  
 177 the computation but we emphasize that there are restrictions on the relative size of the spatial and temporal  
 178 grids in order to obtain reasonable results, namely, an excessively small time step relative to the space grid  
 179 size leads to incorrect stagnation of moving level sets. A common practice is to take  $\delta t$  proportional to

180 the first power of the spatial grid size (Misiats and Yip, 2016). Moreover, the parameter  $\varepsilon$  of the auction  
 181 algorithm is taken as a small positive value and has the role of preventing a "price war" infinite loop, where  
 182 the prices  $p_i$  get stuck at a certain value. Too small  $\varepsilon$  may result in an increase in computational time,  
 183 while a large value may lead to deviations from the prescribed cell volumes. The complexity of the auction  
 184 step is  $O(Nv(\log v + N)C/\varepsilon)$ , where  $v = \max_i v_i$  and  $C = \max_{i,x} \psi_i^k(x)$ , but implementing a scaling in this  
 185 parameter improves both computational time and accuracy (Jacobs et al., 2018).

186 We summarize basic mathematical properties of the algorithm, i.e., its stability and convergence. Firstly,  
 187 for the original algorithm without volume constraint, Esedoğlu and Otto (2015) showed that it is uncondi-  
 188 tionally gradient stable: for any choice of the time step  $\delta t$ , it dissipates in every time step the approximate  
 189 energy (A.4) (which  $\Gamma$ -converges to the energy (1)) under the sufficient condition that the surface tension  
 190 matrix  $\{\sigma_{ij}\}_{i,j=1}^N$  is conditionally negative semidefinite:

$$\sum_{i,j=1}^N \sigma_{ij} \xi_i \xi_j \leq 0 \quad \text{for any } (\xi_1, \dots, \xi_N) \in \mathbb{R}^N \text{ such that } \sum_{i=1}^N \xi_i = 0. \quad (5)$$

191 This condition is often satisfied in materials science but there is no guarantee that it will hold in biological  
 192 settings, e.g., cell-cell adhesiveness strengths in olfactory epithelium measured in terms of its  $\beta$ -catenin  
 193 intensity values (Katsunuma et al., 2016). In such a case, it is possible to devise a slightly more complex  
 194 version of the algorithm that guarantees gradient stability solely under the  $\sigma$ -triangle inequality condition.  
 195 We refer to Section 5.4 of (Esedoğlu and Otto, 2015) for details. The convergence of the algorithm to the  
 196 weak solution of the  $L^2$ -gradient flow of the energy (1) has been proved in (Laux and Otto, 2016). We  
 197 note that due to the fundamental idea of the algorithm to propagate interfaces over a fixed grid and due  
 198 to the stagnation phenomenon mentioned above, the order of convergence is restricted to at most 1 in both  
 199 time and space, while the order near multiple junctions turns out to be only  $\frac{1}{2}$  in time. Analogous results  
 200 on stability and convergence hold also for the volume-preserving version of the Esedoğlu-Otto algorithm,  
 201 i.e., the minimization problem (2). Stability can be obtained by a simple modification of the original proof  
 202 (see (Xu et al., 2017) for the basic idea) and convergence has been established in (Laux and Swartz, 2017).  
 203 Finally, the convergence of the auction algorithm is well-known (see the references in (Jacobs et al., 2018)).  
 204 It follows that the localized auction scheme is justified locally, but analysis of its global behavior is still  
 205 missing.

206 In this section, we have presented an algorithm that can express arbitrary curved shapes of cellular  
 207 junctions thanks to its being rooted in the level set approach. In the following two sections, we address the  
 208 remaining two benefits of our algorithm announced at the end of the introductory section: small number of  
 209 parameters (Section 3), and natural treatment of topology changes (Section 4).

### 210 3. Parameters of the Algorithm

211 Besides the parameters  $m$ ,  $\delta t$ , and  $\varepsilon$ , used in the numerical implementation of the model, the only  
212 parameters of the model itself are the weights  $\sigma_{ij}$ , showing a major advantage over other similar models.  
213 For example, the vertex dynamics model includes, besides these weights, several further parameters, such as  
214 the elastic stiffness coefficients for the volume and perimeter, minimal distance of two vertices to initiate T1  
215 transformation, a parameter for the resulting distance of the vertices, etc. Consequently, our model allows  
216 us to focus on the role of the target force represented by the parameters  $\sigma_{ij}$ , without having to analyze the  
217 impact of other effects. This is essential as such analysis often presents an infeasible task.

218 The choice of specific values for the  $\sigma_{ij}$ 's depends on the purpose of the modeling, and usually requires  
219 novel ideas and insights into the modeled phenomenon. Moreover, these values are the only doorway through  
220 which results of experimental measurements can be reflected in the model in a quantitative manner, and  
221 thus their choice is also closely tied to the design of experiments. In this sense, it is impossible to devise a  
222 general recipe, and we will only give some examples of the possible choices for  $\sigma_{ij}$ 's.

223 There are two basic competing approaches to the design of the weights  $\sigma_{ij}$ , which, as we believe, are peace-  
224 fully united in our model: Steinberg's differential adhesion hypothesis (Steinberg, 1963; Foty and Steinberg,  
225 2005), and the differential interfacial tension hypothesis put forward by Brodland (2002). Steinberg (1963)  
226 based his theory on the observation of similarities between liquid sorting and cell sorting, and postulated  
227 that cellular rearrangements can be in certain cases explained by the tendency of the cells to maximize their  
228 intermolecular adhesion. Evidences speaking for the correctness of the hypothesis were provided by several  
229 experiments, the prominent one being the establishment of a hierarchical sequence of segregation among  
230 several different tissues. Later, Brodland (2002) pointed out that adhesion acts in the opposite direction  
231 than interfacial tension, and formulated a more complete and precise hypothesis, giving it a new name. Dis-  
232 cussions in the biological modeling community on the significance of these and other hypotheses have been  
233 conducted for several decades (Harris, 1976; Brodland, 2004). Our purpose here is not necessarily to probe  
234 into these discussions; but rather to present a general model that can encompass most of the approaches  
235 proposed up to date. For example, the model can take the weights  $\sigma_{ij}$  to be the cortical tensions of the cell  
236 membrane (Maître et al., 2015) (in which case there is a direct correspondence with the physical meaning of  
237 these parameters), or the weights may reflect the adhesion energy per area (Katsunuma et al., 2016; Maître  
238 and Heisenberg, 2011) (in which case  $\sigma_{ij}$ 's do not have the meaning of adhesion energy but depend on that  
239 energy in a suitable manner that has to be determined as a part of the particular model), or a combination  
240 of both. In Section 6, we give a specific example of the design of the weights  $\sigma_{ij}$  that express the adhesion  
241 energy and are quantified through the experimentally measurable quantity of  $\beta$ -catenin intensity.

242 We would like to bring attention to the fact that the weights  $\sigma_{ij}$  in the algorithm can be time-dependent,  
243 which is expressed by the index  $k$  in equation (3). This is essential, as almost all morphogenetic phenomena  
244 are driven by temporally changing forces. Moreover, this time-dependence turns our model from a mere  
245 energy minimizing gradient descent system into an out-of-equilibrium one, as expected for a model of a

246 living system.

247 The minimal set of parameters, i.e., the weights  $\sigma_{ij}$ , can be augmented by new parameters according to  
248 necessity to express various additional aspects of the target biological phenomenon. One example of such  
249 additional parameters are the mobilities  $\mu_{ij}$  mentioned in the beginning of Section 2. In fact, the algorithm  
250 as presented in Section 2 advances each junction  $\gamma_{ij}$  with the mobility  $\mu_{ij} = 1/\sigma_{ij}$ . If one wishes to prescribe  
251 mobilities in a different way, it is possible to modify the algorithm by introducing so-called retardation  
252 terms, as explained in Section 5.1 of (Esedoğlu and Otto, 2015). This method was improved in (Salvador  
253 and Esedoğlu, 2019) by replacing the computation of retardation functions by a more efficient convolution  
254 step.

255 Another optional set of parameters  $\{a_i^k, b_i^k\}_{i=1}^N$  is related to the lower and upper bounds controlling the  
256 volumes of individual cell regions, in the sense that we look for the energy minimizing configuration such  
257 that the discrete cell volumes  $v_i^k$  (i.e., the number of grid points in cell  $\mathcal{C}_i$  at a given time  $t_k$ ) satisfy

$$a_i^k \leq v_i^k \leq b_i^k, \quad i = 1, \dots, N. \quad (6)$$

258 It is possible to modify the auction algorithm to extend it to this type of constraint. The implementation  
259 of the upper bound does not significantly change the algorithm but the lower bound requires running also  
260 a reverse auction where cell regions bid on points (see (Jacobs et al., 2018), Section 3.3). One can also  
261 incorporate random effects in the algorithm - either by randomly changing cell volumes (see (Jacobs et al.,  
262 2018), Section 3.4) or by adding a suitable noise to the weights  $\sigma_{ij}$ .

#### 263 4. On Topological Singularities

264 We conduct numerical experiments to demonstrate that our algorithm can handle various types of topo-  
265 logical singularities. First, we show that the localization scheme resolves the wetting and nucleation problem  
266 of the original Esedoğlu-Otto algorithm. In the second part of this section, we show that our level set-based  
267 approach – inheriting the implicit nature of its predecessors, naturally handles topological changes in tissue  
268 morphogenesis, in particular, due to cellular intercalations.

269 Consider a wetting case for a 4-cell aggregate of three types: 2 blue, 1 red, and 1 gray cell (see Figure  
270 3), with  $\sigma_{BB} = 1.5$ ,  $\sigma_{BC} = 0.5$ , and  $\sigma_{RR} = \sigma_{GG} = \sigma_{BR} = \sigma_{RG} = 1.0$ . Here,  $B, R, G$  denote the cells of  
271 type blue, red and gray, respectively, so that, for example,  $\sigma_{BR}$  means the interfacial energy weight for the  
272 junction between blue and red cell. Note that this violates the triangle inequality, since  $\sigma_{B_1G} + \sigma_{B_2G} =$   
273  $1 < 1.5 = \sigma_{B_1B_2}$ . We evolve the initial configuration using three different algorithms: the original Esedoğlu  
274 and Otto (2015) scheme alone, the same scheme with standard auction dynamics (Jacobs et al., 2018),  
275 and finally with our proposed scheme employing a localized auction dynamics. Here, we discretize domain  
276  $\Omega = [0, 1] \times [0, 1]$  uniformly into  $m = 500 \times 500$  points, prescribe periodic conditions on its boundary, and set  
277 time step size  $\delta t = 0.0005$ . Note that periodic boundary conditions are automatically satisfied when FFT is  
278 employed. Results of the simulation are shown in Figure 3 and Movie S1.

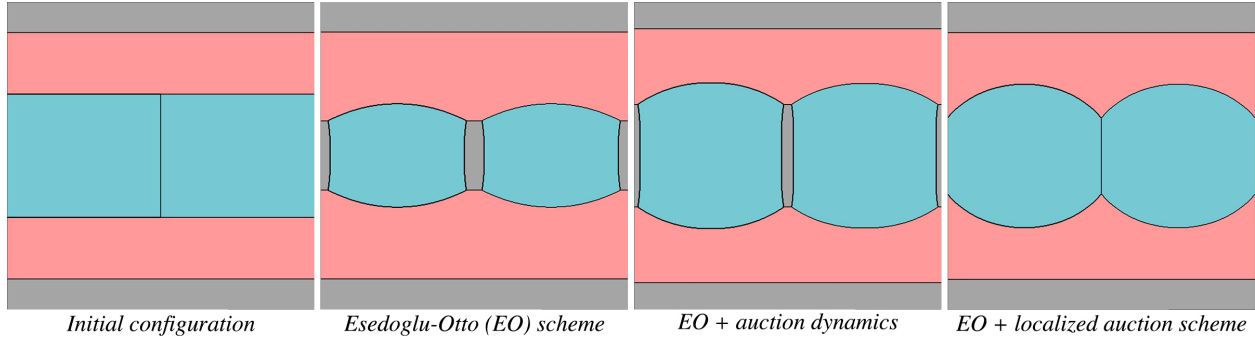


Figure 3: Wetting phenomenon in the numerical implementation of level set-based methods. Initial 4-cell configuration and its evolution under a wetting condition due to violation of  $\sigma$ -triangle inequality at  $t = 50\delta t$  using Esedoğlu-Otto scheme (EO); EO scheme with auction dynamics algorithm; and EO scheme with localized auction dynamics.

279 Observe that for the Esedoğlu-Otto scheme, a new gray cell grows at the  $BB$ -junctions – wetting occurs.  
 280 When implemented with usual auction dynamics, we see that the gray cell splits and some of its parts  
 281 appear in the  $BB$ -junction. In these cases, optimization (2) is taken over all possible cells, and thus  $\sigma$ -  
 282 triangle inequality becomes important to rule out wetting. However, with the localized auction dynamics,  
 283 cell splitting due to wetting is avoided. This is because, for points in the neighborhood of the  $BB$ -junction,  
 284 maximization (4) is localized and only taken over the two blue cells. Hence, irregardless of whether  $\sigma$ -triangle  
 285 inequality holds, wetting does not occur with localized auction dynamics.

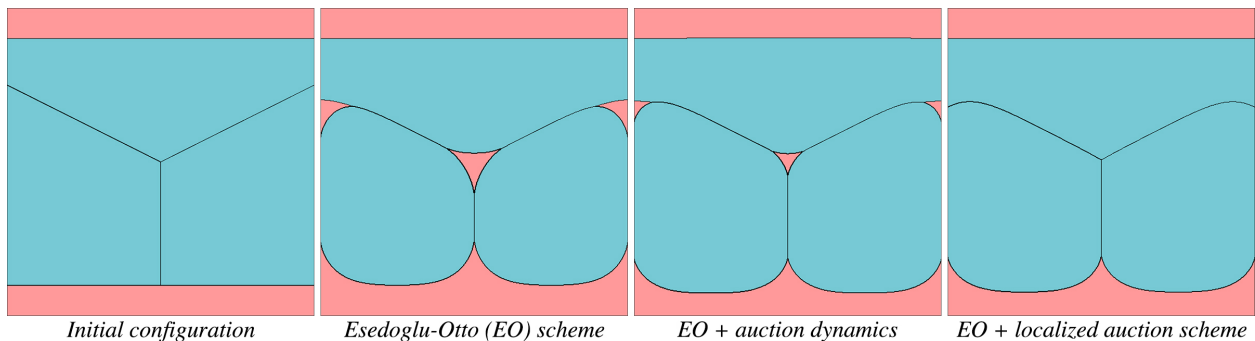


Figure 4: Nucleation phenomenon in the numerical implementation of level set-based methods. Initial 4-cell configuration and its evolution at  $t = 10\delta t$  using Esedoğlu-Otto (EO) algorithm resulting in nucleation of red cell at the blue triple junction; EO scheme with auction dynamics where red cell splitting persists; and EO scheme with localized auction dynamics which preserves cell connectivity.

286 Next, consider a nucleation case for a 4-cell aggregate of two types: 3 blue and 1 red cell (see Figure 4)  
 287 under the same conditions on the domain and time step size as in the first simulation. With  $\sigma_{BB} = \sigma_{RR} = 1.0$   
 288 and  $\sigma_{BR} = 0.530$ , we evolve the initial configuration using the same numerical schemes as above. Note that  
 289 since the  $\sigma_{ij}$ 's satisfy the triangle inequality condition, wetting cannot take place. However, Figure 4 and  
 290 Movie S2 show that in the evolution computed by Esedoğlu-Otto algorithm alone, red cells grow in the

291 vicinity of the blue tricellular junction – an unnatural cell dynamics. This phenomenon persists even when  
 292 auction algorithm is incorporated, but is completely eliminated upon introducing the localization.

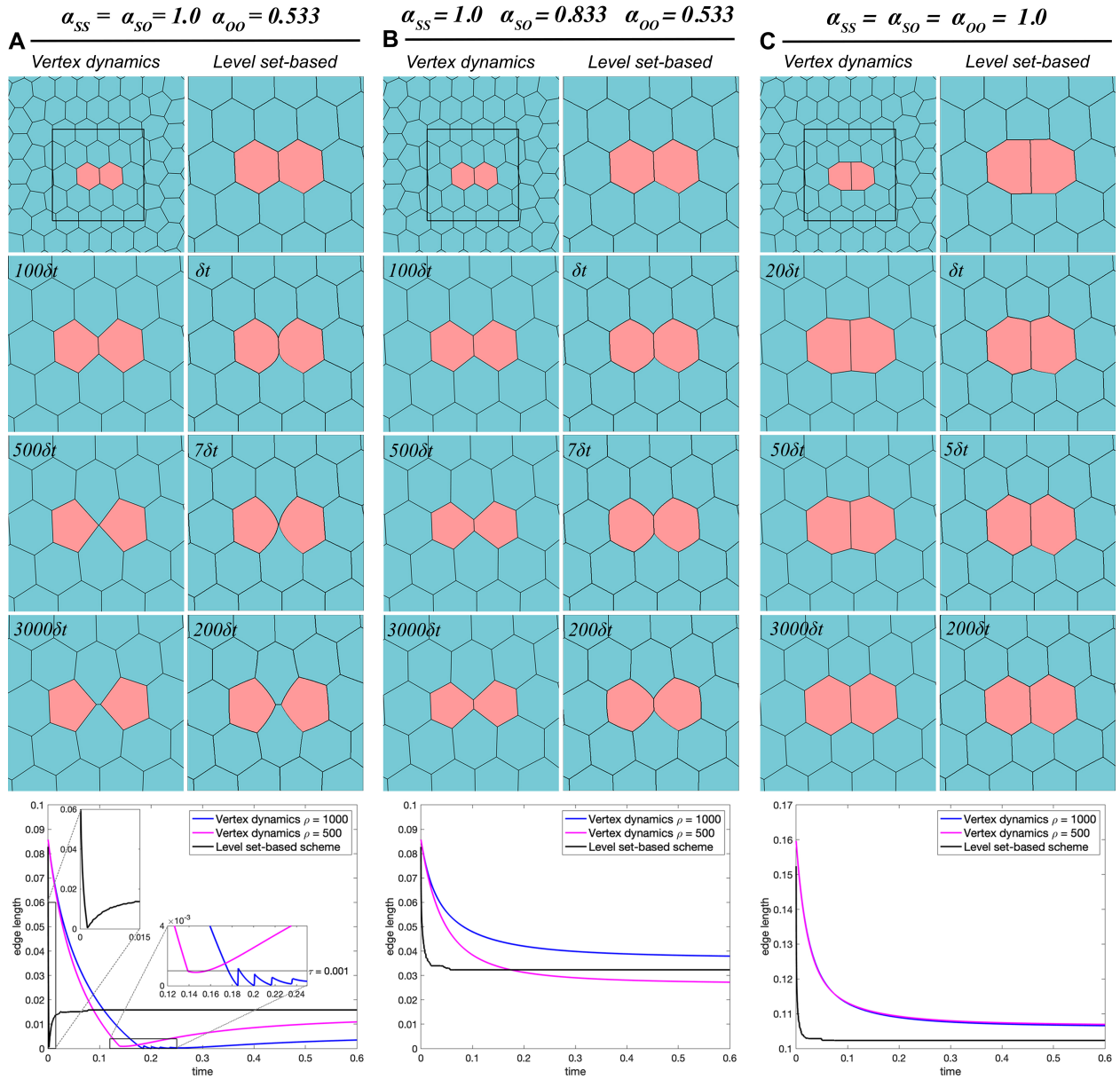


Figure 5: Vertex dynamics vs. Level set-based model. Three test cases of adhesion strengths: (A)  $\alpha_{SS} = \alpha_{SO} = 1.0$  and  $\alpha_{OO} = 0.533$  leading to cellular intercalation; (B)  $\alpha_{SS} = 1.0$ ,  $\alpha_{SO} = 0.833$  and  $\alpha_{OO} = 0.533$  where no intercalation occurs; and (C)  $\alpha_{SS} = \alpha_{SO} = \alpha_{OO} = 1.0$  which shortens OO-junction. Initial aggregate of 62 blue SCs and 2 red OCs (top left), its zoomed-in configuration (top right), and its evolution via vertex dynamics model with  $\rho = 500$  (left column) and level set-based approach (right column) for each case. (Bottom) Plot showing the shrinkage of the OO-junction length (and the formation of a new SS-junction for the case where cellular intercalation occurs), generated using vertex dynamics model (blue and magenta, expressing different volume penalties  $\rho$ ) and our level set-based approach (black) for each case.

293 To highlight the ability of the algorithm to deal with topology changes, such as cell intercalations, let us  
 294 delve into cellular pattern formations in developmental stages in the olfactory epithelium (OE). Katsunuma  
 295 et al. (2016) hypothesized that heterophilic trans-interaction between nectin-2 on olfactory cells (OCs) and  
 296 nectin-3 on supporting cells (SCs) promote recruitment in the cell-cell junction of the cadherin-catenin  
 297 complex whose representative marker,  $\beta$ -catenin indicates the differential adhesions required to drive self-  
 298 organized cell movements in OE. Following the differential adhesion hypothesis (Steinberg, 1963; Foty and  
 299 Steinberg, 2005), Katsunuma et al. (2016) simulated two cases of cellular patterns: one with adhesion  
 300 strengths  $\alpha_{SS} = \alpha_{SO} = 1.0$ , and  $\alpha_{OO} = 0.533$ ; while the other had a weaker adhesion  $\alpha_{SO} = 0.833$ .  
 301 Using the vertex dynamics model with  $\sigma_{ij} = \alpha_{ij}^{-1}$ , they were able to confirm that the first case leads to  
 302 cellular intercalation, while the second does not; thereby, supporting their idea that differential adhesion in  
 303 heterotypic cell-cell junctions drives cell intercalations.

304 In order to compare the performance of the standard vertex dynamics algorithm and our scheme, we  
 305 consider an initial cellular aggregate of 62 SCs (blue) and 2 OCs (red) cells of almost equal volumes, similar  
 306 to that in (Katsunuma et al., 2016), with periodic boundary conditions on the square domain  $\Omega = [0, 1] \times [0, 1]$   
 307 (see Figure 5). We simulate both cases using the vertex dynamics model and our proposed scheme, with  
 308 the same time step size  $\delta t = 0.0003$ . For the vertex dynamics model, we employ the same potential as in  
 309 (Katsunuma et al., 2016) with two types of cell volume penalty ( $\rho = 1000$  and  $\rho = 500$ ) and minimum  
 310 threshold distances  $\tau = 10^{-3}$  for T1-transition. Moreover, for our level set-based approach, we discretize the  
 311 domain uniformly into  $m = 1000 \times 1000$  points. Numerical results are shown in Figure 5 – note here that  
 312 the times where the snapshots are taken at largely different for each method (see also Movies S3, S4, and  
 313 S5).

314 We observe that both methods do lead to cellular intercalation when adhesion strengths  $\alpha_{SS} = \alpha_{SO} = 1.0$ ,  
 315 and  $\alpha_{OO} = 0.533$  are set. However, essential differences are found in the results. First, the time needed for  
 316 the intercalation to occur in the vertex dynamics algorithm heavily depends on the minimum T1-transition  
 317 threshold distance  $\tau$ , which can be seen by following the magenta line in Figure 5A – the edge length starts  
 318 to increase when this line hits the level  $\tau$ . In other words, a small change in  $\tau$  may result in largely different  
 319 times of intercalation, which in turn may have significant impact on the global dynamics of the aggregate.  
 320 Second, and probably the most prominent difference between the two methods lies in the time rate of change  
 321 of the junction length, i.e., the vertex dynamics motion is reluctant to undergo topology changes. Lastly,  
 322 inspecting Figure 5A, it is clear that both methods yield quite different final shapes of the intercalated cells.

323 To confirm whether this aspect of vertex dynamics is pertinent to topology changes such as intercalation,  
 324 we have compared the evolution of junction lengths with cases where no intercalation occurs. Results for one  
 325 such setting are shown in Figure 5B, where the difference in adhesion strengths (having  $\alpha_{SS} = 1.0, \alpha_{SO} =$   
 326  $0.833, \alpha_{OO} = 0.533$ ) drives the OCs towards intercalation but is not strong enough for the intercalation to  
 327 occur. Another test case, depicted in Figure 5C sets all adhesion strengths equal to 1.0 and considers an  
 328 initial configuration with unnaturally long junction between the red cells. One observes that the dynamics

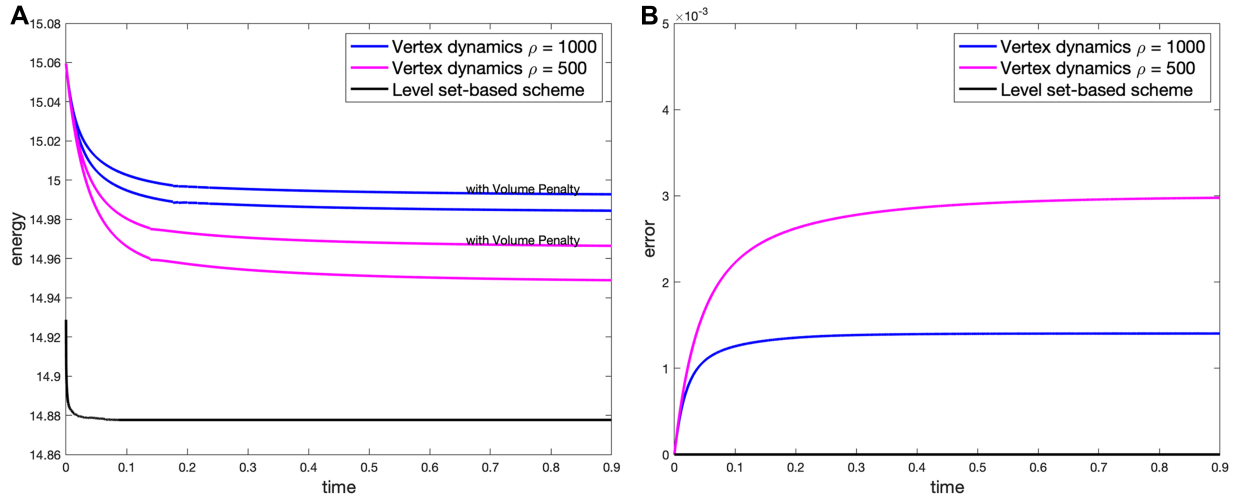


Figure 6: Evolution of energy and cell volumes for the simulation in Figure 5A. (A) The total energy (upper blue curve) and its surface energy component (lower blue curve) of the vertex model for volume penalty  $\rho = 1000$  and analogous results for penalty  $\rho = 500$  (magenta). The black line shows the evolution of energy of level set-based method. The discrepancy in initial energy for both methods is caused by the different representation of cell shapes. (B) The evolution of cell volume error defined at time  $t_k$  as the maximum absolute deviation of cell volumes from the prescribed volume, where the volume is calculated as polygonal area in the vertex dynamics model, and by  $v_j^k(\Delta x)^2$  in the level set based model.

329 in this last case is similar for both methods leading to approximately the same stationary junction length,  
 330 although the vertex dynamics model evolves slightly slower. In the “almost intercalating” test case of Figure  
 331 5B, the vertex dynamics model lags behind the level set-based scheme and converges to a significantly  
 332 different stationary length of the junction, which also strongly depends on the parameters of the vertex  
 333 dynamics model, in this case, the volume penalty. Meanwhile, in all test cases, the level set-based algorithm  
 334 swiftly approaches the steady state configuration, irregardless of the presence of intercalation, as expected  
 335 from its convergence proof. From these findings, we may conclude that vertex dynamics model tends to slow  
 336 down the evolution when topology changes are to take place, contrary to what is expected from the energy  
 337 minimization principle.

338 This difference between the models is mainly caused by three factors, as follows. The first one is due  
 339 to the different form of their energies, since the vertex model includes not only the surface energy but also  
 340 other terms such as volume penalty term, etc. Secondly, the correct cell contact angles are not realized in the  
 341 vertex dynamics model particularly for curved cell-cell junctions, which may alter succeeding cell dynamics.  
 342 This, on the contrary, does not occur in the level set-based approach, as it is theoretically proved to satisfy  
 343 the tricellular angle condition. Lastly, the vertex dynamics model can only take a restricted set of paths  
 344 to minimize its energy. Indeed, since the level set-based method allows for arbitrary shapes of junctions,  
 345 contrary to the vertex model where only polygonal shapes are allowed, it is able to follow the gradient descent  
 346 of the energy correctly; while the vertex dynamics model is delayed (and for some cases, completely stopped)

347 by having to take only polygonal deformations.

348 We elaborate on the first difference mentioned in the previous paragraph. In our model, the energy  
349 consists only of surface energy, and the volume preservation is realized through the constraint condition.  
350 Thus, the cell sizes are preserved precisely. On the other hand, in the vertex model, the energy is defined  
351 as the sum of surface energy and volume penalty term, while it is necessary to use a large value of penalty  
352 coefficient  $\rho$  in order to preserve the cell sizes to some extent. The effect of the surface energy term is then  
353 relatively weakened when  $\rho$  is large. In this way, the level set-based approach allows us to focus on the  
354 effect of surface or adhesion energy, unlike the vertex model where it is difficult to separate and correctly  
355 understand this effect (see Figure 6). This provides a typical example of the importance of reducing model  
356 parameters: the vertex model does not facilitate the understanding of the adhesion mechanism because the  
357 influence of its two additional parameters, namely the volume penalty coefficient  $\rho$  and threshold distance  
358 for T1 transition  $\tau$ , cannot be easily analyzed. Indeed, as one can see in Figure 5A, mere doubling of the  
359 volume penalty coefficient  $\rho$  leads to a completely different behavior of the edge length. The oscillations  
360 of the edge length for the stronger volume penalty represent a tug of war triggered by the T1 transition  
361 between the elastic volume term and the surface adhesion term in the energy.

362 To conclude this section, we remark on some computational aspects of the level set-based method. First,  
363 we discuss the jump-like behavior of the junction length in the level-set based method, which the reader might  
364 have noticed in Figures 5 and 6. This is due to fact that the level set method is performed on a fixed grid  
365 causing sudden changes of the length as a tricellular point jumps from one grid cell to another. On the other  
366 hand, the meshless vertex dynamics moves the tricellular points freely in space and hence yields smoothly  
367 changing lengths. However, the jumps observed in the level-set based method diminish with the refinement of  
368 the grid. Second remark concerns computational cost of the level set-based method. Contrary to the vertex  
369 dynamics, where the  $x, y$ -coordinates of the vertices are the only degrees of freedom, the level set method  
370 requires determining functional values at every point of the two-dimensional grid. Therefore, the level set  
371 method solves a higher-dimensional discrete problem, and in this sense is expected to have theoretically  
372 higher computational cost, especially on fine grids. Meanwhile, as the partial differential equation to be  
373 solved is a simple heat equation, the application of FFT allows its fast solution, as detailed in Section 2.  
374 Moreover, the intercalation example of Figure 5A shows that the correct realization of gradient flow by the  
375 level set methods requires significantly smaller number of time steps to reach the equilibrium compared to  
376 the stiff evolution by vertex dynamics. Hence, the theoretically higher computational cost does not always  
377 imply longer computational time needed to reach the required solution.

## 378 5. Cellular Mosaic Patterns

379 In the remaining part of the paper, we present several specific examples of morphogenetic phenomena in  
380 order to show the wide applicability of the proposed model and numerical algorithm. We begin by phenomena  
381 that have already been treated more or less successfully by other methods, namely cell sorting as an example

382 of pattern formation, and cell internalization as an example of a phenomenon including a medium. The  
 383 main contribution of this part, however, is the application of our method to the formation of mosaic and  
 384 checkerboard patterns in sensory epithelia, a problem that has been withstanding the challenges of existing  
 385 models.

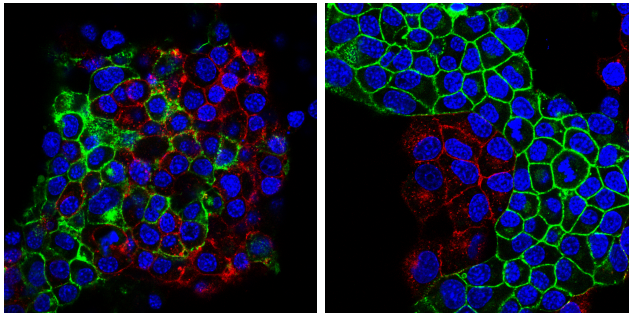


Figure 7: Two different cell sorting mechanisms. (Left) The mosaic pattern of the mixed culture of cells expressing different nectins (green: nectin-1 (AF297665.1); red: nectin-3 (NM\_021495.4); blue: cell nucleus). (Right) The segregated pattern of the mixed culture of cells expressing different cadherins (green: N-cadherin (NM\_007664.5); red: E-cadherin (NM\_009864.3); blue: cell nucleus)

386 Among the phenomena that occur in a heterotypic aggregate of embryonic cells are cell sorting, mixing,  
 387 and formation of checkerboard patterns. In epithelial tissues, for example, when cells expressing different  
 388 types of cadherin – a homophilic cell adhesion molecule – are mixed, these cells form separate aggregates  
 389 (Nose et al., 1988). Similar segregation of cells occurs if cells expressing different amounts of the same  
 390 cadherin are mixed (Steinberg and Takeichi, 1994). From these observations, cadherin quantity and affinity  
 391 are thought to control tissue segregation and assembly. In contrast to cadherins, nectins prefer heterotypic  
 392 binding to homotypic one, and their heterophilic interactions produce stronger cell-cell adhesions than their  
 393 homophilic interactions. Owing to these properties of nectins, cells in mixed cultures expressing different  
 394 nectins became arranged in a mosaic pattern (Togashi et al., 2011) (see Figure 7).

395 Cell sorting begins with the formation of smooth chains of cells, followed by shortening of these chains  
 396 into round masses, and finally annealing of the resulting masses (Brodland and Chen, 2000; Brodland and  
 397 Veldhuis, 2002). This has been studied by Brodland (2002) from the viewpoint of the differential interfacial  
 398 tension hypothesis, where self-rearrangement of embryonic cells and tissues are driven by differences in  
 399 interfacial tensions. Finite element-based simulations in (Brodland and Chen, 2000; Brodland and Veldhuis,  
 400 2002; Brodland, 2004) showed that for an aggregate of two cell types, say, blue and red cells, sorting occurs  
 401 only when interfacial tensions satisfy  $\sigma_{BR} > \frac{1}{2}(\sigma_{BB} + \sigma_{RR})$ ; meanwhile a sufficient condition for mixing is  
 402  $\sigma_{BR} < \frac{1}{2}\sigma_{BB}$  or  $\sigma_{BR} < \frac{1}{2}\sigma_{RR}$ .

403 We recreate these simulations using our level set-based approach. Consider an initial aggregate of 50  
 404 similar-sized cells where cell types are randomly assigned to 25 blue and 25 red cells (see Figure 8 and Movie  
 405 S6). We discretize the domain  $\Omega = [0, 1] \times [0, 1]$  uniformly into  $m = 300 \times 300$  points, consider periodic

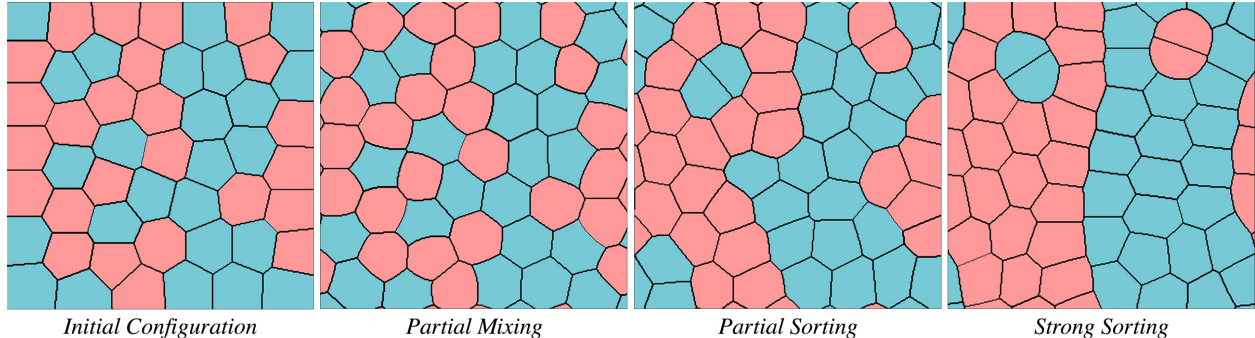


Figure 8: Cell sorting via level set-based model. Initial aggregate of 25 blue and 25 red cells with interfacial tensions  $\sigma_{BB} = 0.6$  and  $\sigma_{RR} = 1.0$ ; its evolution generated by the level set-based approach for partial mixing when  $\sigma_{BR} = 0.7$ ; partial sorting when  $\sigma_{BR} = 1.1$ ; and strong sorting when  $\sigma_{BR} = 2.0$ .

406 boundary conditions, and set time step size  $\delta t = 0.0008$ . In this setup, we take interfacial tensions  $\sigma_{BB} = 0.6$   
 407 and  $\sigma_{RR} = 1.0$  over 300 time steps (cf. (Brodland, 2002)). Observe that when  $\sigma_{BR} = 0.7$ , partial mixing of  
 408 blue and red cells occurs. Moreover, increasing this interfacial tension to  $\sigma_{BR} = 1.1$  leads to partial sorting  
 409 of different cell types; and further increasing to  $\sigma_{BR} = 2.0$  results in strong sorting. Hence, our method  
 410 is able to produce similar results as those of the finite element-based simulations in Figure 5 of (Brodland,  
 411 2002). The only difference is that our level set-based method naturally handles topological changes; while  
 412 this FEM-based approach requires an ad hoc scheme, in particular, a boundary "flip" algorithm (Brodland,  
 413 2004) to handle cellular intercalations, which may cause some problem for certain cellular configurations, in  
 414 the same way as in the vertex dynamics model.

415 On the other hand, employing the viewpoint of differential adhesion hypothesis, Katsunuma et al. (2016)  
 416 hypothesized that relative intensities of  $\beta$ -catenin accumulations in mixed cultures of cells expressing nectin-  
 417 2 and N-cadherin (blue cells in Figure 9) with various transfectants (red cells in Figure 9) lead to different  
 418 mosaic cellular patterning. In particular, a segregated pattern is formed when mixed with cells expressing  
 419 nectin-2, N-cadherin, and E-cadherin where the adhesion strengths satisfy  $\alpha_{RR} > \alpha_{BR} > \alpha_{BB}$ ; a checker-  
 420 board pattern when mixed with cells expressing nectin-3 and N-cadherin resulting in  $\alpha_{BR} > \alpha_{RR} = \alpha_{BB}$ ;  
 421 and a football (kagome) pattern when mixed with cells expressing nectin-3, N-cadherin, and E-cadherin  
 422 where  $\alpha_{BR} = \alpha_{RR} > \alpha_{BB}$ . To confirm these hypothetical profiles of synergistic actions of nectins and cad-  
 423 herins on cellular patterning, we use our level set-based scheme and simulate the corresponding cell motions.  
 424 In our simulations involving adhesion as the physical parameter, we always set the coefficients  $\sigma$  in (1) as  
 425 the reciprocal of the cell-cell adhesion strength  $\alpha$ , i.e.,  $\sigma = \alpha^{-1}$ .

426 Consider an initial 48-cell aggregate where cell types are randomly assigned to 24 blue and 24 red cells (see  
 427 Figure 9 and Movie S7). We consider a computational domain  $\Omega = [0, 1] \times [0, 1]$  discretized uniformly into  
 428  $m = 300 \times 300$  points and set time step size  $\delta t = 0.0008$ . On the left and right boundaries, we impose periodic  
 429 boundary conditions; while on the top and bottom boundaries, we prescribe a fixed adhesion strength of  
 430 0.10. Moreover, we consider time-dependent cell-cell adhesion strengths, which change piecewise linearly in

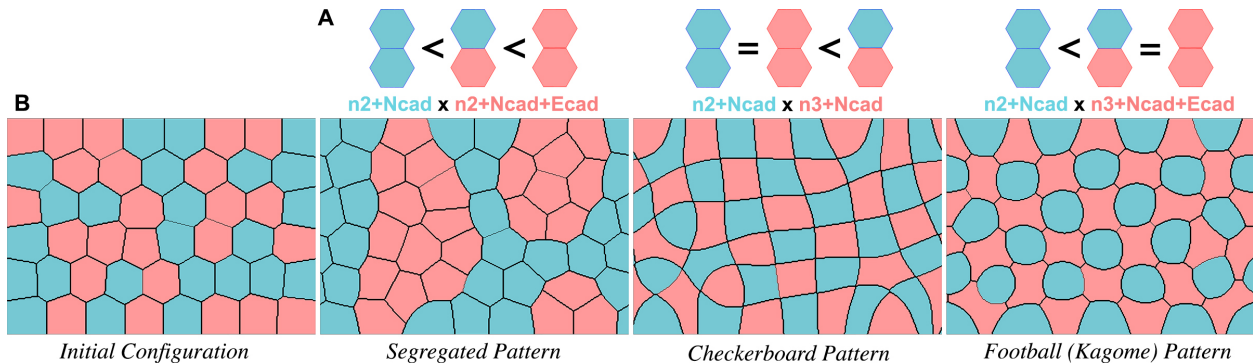


Figure 9: Cellular patterns via level set-based model according to hypothetical profiles of synergistic actions of nectins and cadherins. (A) Schematic diagrams of the relative intensities of the  $\beta$ -catenin accumulations (corresponding to relative adhesion strengths) in mixed cultures of various transfectants, resulting in different mosaic patterns. (B) Initial 48-cell aggregate consisting of 24 blue cells expressing nectin-2 and N-cadherin; and its evolution via level set-based approach resulting in different mosaic patterns: a segregated pattern with red cells expressing nectin-2, N-cadherin, and E-cadherin; a checkerboard pattern with red cells expressing nectin-3 and N-cadherin; and football (kagome) pattern with red cells expressing nectin-3, N-cadherin, and E-cadherin.

431 time starting from  $\alpha_{BB} = \alpha_{BR} = \alpha_{RR} = 1.0$  over 1200 time steps. Observe that when adhesion strengths are  
 432 changed to  $\alpha_{BB} = \alpha_{BR} = 0.50$  and  $\alpha_{RR} = 4.0$ , the blue and red cells segregate creating a final configuration  
 433 similar to that produced by cell sorting. In particular, since  $\alpha_{RR}$  is large, the red cells strongly adhere to  
 434 each other and sort out the blue cells.

435 Moreover, for target adhesion strengths  $\alpha_{BB} = \alpha_{RR} = 1.0$  and  $\alpha_{BR} = 3.0$ , the stationary solution forms  
 436 a checkerboard pattern. Note that a perfect checkerboard pattern is not attained due to the topological  
 437 limitations near the boundary but red and green cells are still distributed in a fully alternating pattern.  
 438 Finally, changing adhesion strengths to  $\alpha_{BB} = 1.0$  and  $\alpha_{BR} = \alpha_{RR} = 3.0$  results in a football pattern.  
 439 However, since there are equal number of cells for each type, only four blue cells surround each red cell and  
 440 vice versa. If the initial aggregate has more red cells, enough for six of them to surround one blue cell, the  
 441 final pattern will be much closer to the standard football pattern.

## 442 6. Developmental Stages in Sensory Epithelia

443 In this section we introduce novel simulation results showing the high potential of the level set method.  
 444 Namely, we focus on the problem of cellular pattern development in sensory organs and reproduce experi-  
 445 mentally observed cell patterns of olfactory and auditory epithelia. As mentioned above, formation of such  
 446 patterns involves curved cell junctions, significantly different sizes of participating cells and frequent topol-  
 447 ogy changes. These aspects present formidable challenges to numerical methods and have not yet been  
 448 overcome. The level set approach is successful not only because it allows for a wide range of geometrical  
 449 patterns but also because it precisely expresses junction contact angles, which is indispensable for realizing

450 cellular intercalation processes correctly.

451 Vertebrates possess highly developed sense organs, responsible for detecting information about different  
 452 environments and converting extracellular stimuli into electrical signals which are mediated by specialized  
 453 sensory epithelia (Togashi, 2016). Mosaic cellular patterns that have been observed in embryonic sensory  
 454 tissues, such as the checkerboard pattern in a mouse auditory epithelium (Togashi et al., 2011) and football  
 455 patterns in postnatal olfactory epithelium (Katsunuma et al., 2016), are evolutionary conserved among a  
 456 wide range of species and thought to be important in sensory functions. For example, the auditory epithelium  
 457 is composed of mechanosensory cells, known as hair cells, equipped with stereocilia that sense sound, and  
 458 supporting cells that separate and help the hair cells. These cells are regularly distributed, and the mosaic  
 cellular pattern is believed to be important for the precise detection of sound signals.

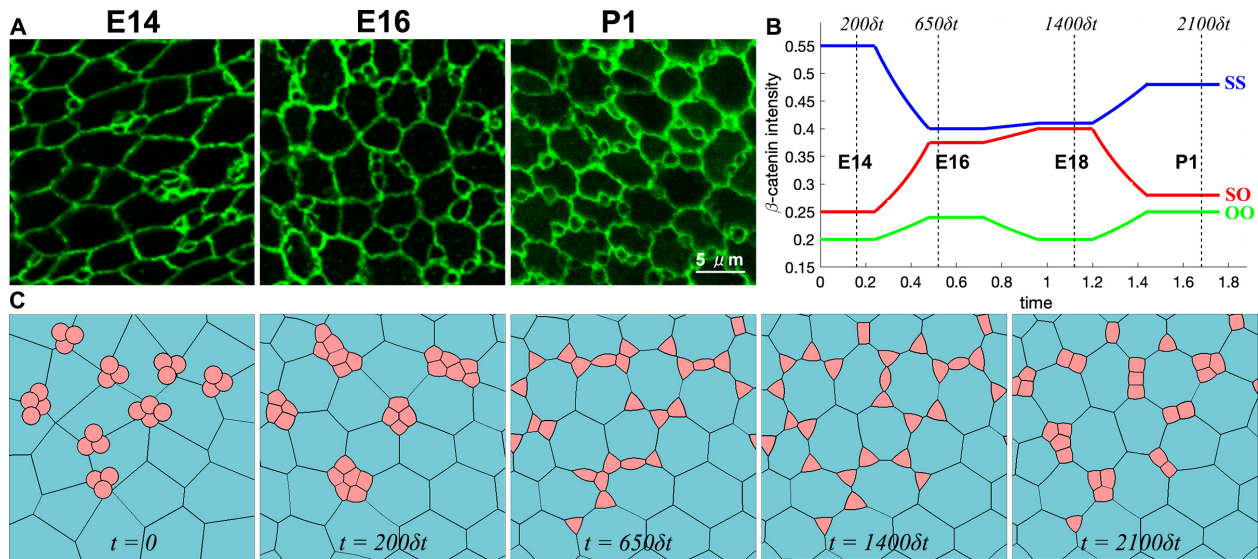


Figure 10: Actual images and simulation results of a developing olfactory epithelium. (A) Immunostaining for junctional marker (ZO-1) on the apical surface of the mouse OE from embryonic days (E14, E16) to postnatal day (P1) (©2016 Katsunuma et al., originally published in Journal of Cell Biology). Most of the olfactory cells first attach to each other during the E14 and E16 stages. As development progresses, olfactory cells separate from one another and each becomes completely surrounded by supporting cells at P1. (B) Plot of relative intensity of  $\beta$ -catenin accumulations at OO, SO, and SS junctions during development based on measurements in (Katsunuma et al., 2016). The graphs were obtained by linear interpolation of  $\beta$ -catenin intensity mean values at time instants E14, E16, E18 and P1 reported in Figure S2 of (Katsunuma et al., 2016). Moreover, the initial (E14) and final (P1) values were kept constant until the cellular pattern equilibrated. (C) A simulation of cellular rearrangement of an olfactory epithelium from initial aggregate of 26 red OCs and 24 blue SCs to embryonic stages E14, E16, E18 until postnatal P1 stage obtained by the level set-based model.

459

460 Using the distributional patterns of  $\beta$ -catenin intensities measured in (Katsunuma et al., 2016), we can  
 461 then apply our level set-based approach to simulate cellular rearrangements in the olfactory epithelium from  
 462 embryonic E14 stage to postnatal P1 stage. Consider an initial aggregate of 26 OCs (red) and 24 SCs (red)

463 on a square domain  $\Omega = [0, 1] \times [0, 1]$  with periodic boundary conditions. We discretize the domain uniformly  
 464 into  $m = 500 \times 500$  points and take time step size  $\delta t = 0.0008$ . As observed in biological experiments, OCs  
 465 are approximately 10 times smaller in size than SCs and tend to cluster around tricellular SC junctions  
 466 during the embryonic day 14 (E14) stage (see Figure 10A). Here, we take  $\sigma$  as the reciprocal of cell-cell  
 467 adhesion strength, measured in terms of  $\beta$ -catenin intensity.

468 Figure 10C and Movie S8 show the simulation of cellular rearrangement of a developing olfactory epithe-  
 469 lium based on  $\beta$ -catenin intensities as adhesion strengths through its developmental stages. Comparing this  
 470 to biological experiments, we see that the level set-based model was able to capture overall cellular rearrange-  
 471 ments in the embryonic stage. In particular, at E14 stage, the olfactory cells cluster at the tricellular SC  
 472 junctions; then from E16 to E18, the olfactory cells separate and move along supporting cell-cell junctions.  
 473 However, it is noticeable that the OCs are not as round as in the experimental results, and are located at  
 474 tricellular SC junctions. This means that in the postnatal stage  $\beta$ -catenin is not the only contributing factor  
 475 for cellular rearrangement in olfactory epithelium.

476 In a developing auditory epithelium, hair cells (HCs) and supporting cells form a checkerboard pattern  
 477 at embryonic E16 stage, such that each hair cell is separated from another hair cell by a supporting cell; and  
 478 later rearrange to a football pattern at embryonic E18 stage (Togashi et al., 2011; Togashi, 2016) (see Figure  
 479 11A,B). Since quantitative experimental measurements of concentrations of adhesive molecules are not yet  
 480 available, we choose hypothetical values for adhesion strengths to generate the cellular rearrangement of an  
 481 embryonic auditory epithelium using our level set-based approach. Consider an initial cellular aggregate  
 482 of 12 HCs (red), 12 SCs (blue), and 16 pillar cells (gray) on a rectangular domain  $\Omega = [0, 1] \times [0.15, 0.85]$   
 483 with periodic boundary conditions (see Figure 11C). As observed in biological experiments, the pillar cells  
 484 are aligned at the top and bottom of the computational domain. We discretize the domain uniformly into  
 485  $m = 480 \times 300$  points, set time step size  $\delta t = 0.0008$  and initial adhesion strengths  $\alpha_{SS} = \alpha_{SH} = \alpha_{HH} =$   
 486  $\alpha_{PS} = \alpha_{PH} = 1.0$  and  $\alpha_{PP} = 7.0$ . Changing only the SC-HC adhesion strength linearly to  $\alpha_{SH} = 5.0$  over  
 487 200 time steps produces a checkerboard pattern as expected in embryonic E16 stage. Moreover, changing  
 488 linearly further to  $\alpha_{SS} = 3.5$ ,  $\alpha_{SH} = 2.5$  and  $\alpha_{PS} = 1.5$  over 200 time steps results in a football (kagome)  
 489 pattern as in embryonic E18 stage (see Figure 11C and Movie S9).

## 490 7. Total Engulfment and Cellular Internalization

491 We conclude the list of applications with two morphogenetic phenomena including a medium that were  
 492 already treated by other methods, and show that our method is able to obtain at least comparable outputs.  
 493 First, consider the case where there are two masses of cells, say, red and blue, and a medium. Following  
 494 the viewpoint of differential interfacial tension hypothesis, Brodland and Chen (2000) proposed that for the  
 495 blue cell mass to be enveloped by the red cell mass, a sufficient condition is  $\sigma_{BR} < \sigma_{BM} - \sigma_{RM}$ . Moreover,  
 496 for such engulfment to continue, it is necessary to have  $\sigma_{BR} < \sigma_{BM}$  (Brodland, 2002).

497 With this in mind, consider an initial configuration of 10 blue cells, 40 red cells, and a gray medium on

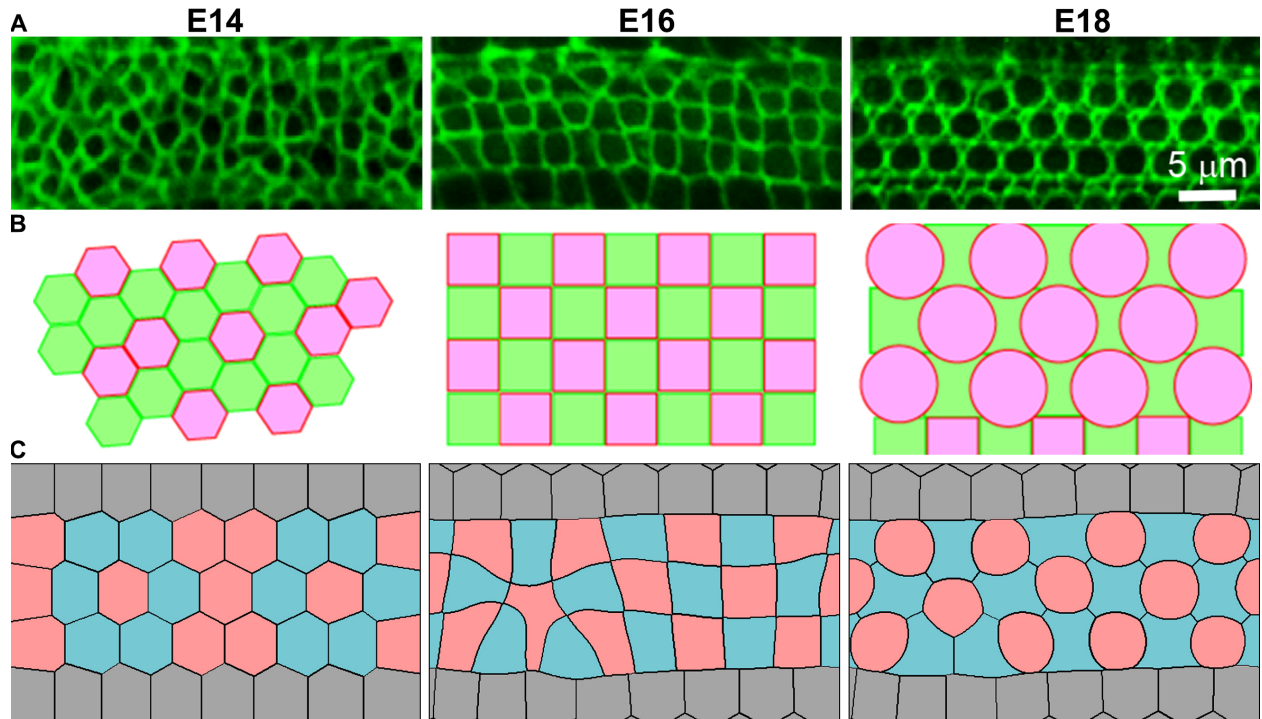


Figure 11: Actual images and simulation results of a developing auditory epithelium. (A) Localization of junctional marker (ZO-1) at the apical surface of the auditory epithelium at embryonic days E14, E16, and E18 (©2016 Togashi, originally published in *Frontiers in Cell and Developmental Biology*). In the developing auditory epithelium, the hair cells and supporting cells continue to change their position and alignment. At P18, the hair cells are arranged in ordered rows, and each hair cell is separated from one another by a supporting cell, forming an alternating mosaic in a checkerboard-like fashion. (B) Schema of the distribution of hair cells (HC, pink) and supporting cells (SC, green) observed in experiments (Togashi, 2016). (C) A simulation of cellular rearrangement of an embryonic auditory epithelium from initial aggregate of 12 red HCs, 12 blue SCs, and 16 gray pillar cells generated employing level set-based model.

498 a computational domain  $\Omega = [0, 1] \times [0, 1]$  discretized uniformly into  $m = 500 \times 500$  points with periodic  
 499 boundary conditions. We take  $\sigma_{BB} = \sigma_{RR} = 1.0$ ,  $\sigma_{BM} = 7.5$ ,  $\sigma_{RM} = 3.5$  and linearly change  $\sigma_{BR}$  from  
 500 7.5 to 2.5 over 100 time steps, keeping  $\sigma_{BR} = 2.5$  for the remaining time of the simulation (cf. (Brodland,  
 501 2002)) and generate its evolution using our level set-based scheme with time step size  $\delta t = 0.001$ . Observe  
 502 that the final configuration results in total engulfment of the blue cell mass by the red cell mass (see Figure  
 503 12 and Movie S10). This is consistent with theoretical considerations that in order to reduce the energy of  
 504  $BR$ -junction, the engulfed blue mass becomes perfectly circular; as well as, the outside engulfing red mass.  
 505 Note that this is not easily achieved by finite element-based simulations, cf., Figure 8 of (Brodland, 2002)  
 506 which yield quite unnaturally distorted shapes of cells, particularly, in the region where the blue cell mass  
 507 is engulfed by the red cell mass. This is because, as a variation of the vertex dynamics model, cellular  
 508 intercalations in the FEM-based approach are explicitly treated using an ad hoc boundary "flip" algorithm.

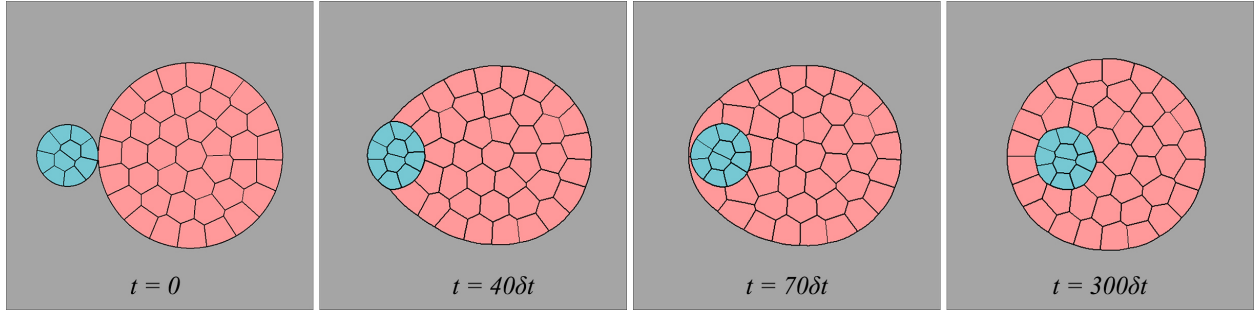


Figure 12: Total engulfment via level set-based model. An initial aggregate of 10 blue and 40 red cells surrounded by a medium and its evolution generated by our level set-based model, resulting in the total engulfment of the blue cell mass by the red cell mass where the interfacial tensions are  $\sigma_{BB} = \sigma_{RR} = 1.0$ ,  $\sigma_{BM} = 7.5$ ,  $\sigma_{RM} = 3.5$ , and  $\sigma_{BR}$  linearly changing from 7.5 at time  $t = 0$  to 2.5 at time  $t = 100\delta t$  and then kept constant.

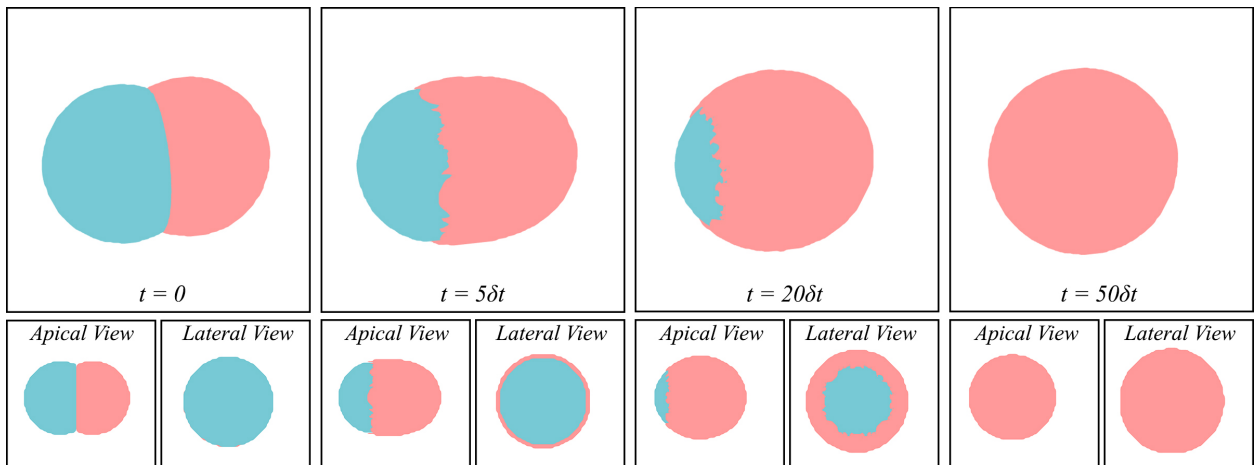


Figure 13: Cell internalization via level set-based model. An initial cell doublet configuration and its evolution (top) using a level set-based approach with interfacial tensions  $\sigma_{BM} = 2.05$ , and  $\sigma_{RM} = \sigma_{BR} = 1.0$ ; and their corresponding apical and lateral views (bottom).

509 Next, we look into embryo morphogenesis where mammalian embryo self-organizes into a blastocyst,  
 510 consisting of epithelial layer encapsulating the inner-cell mass (Maître et al., 2015). Since asymmetrically  
 511 divided 8-cell-stage blastomeres encompass both the morphogenesis and fate specification of the whole em-  
 512 bryo, it is enough to consider a cell doublet as an initial configuration, which results in the red cell enveloping  
 513 its neighboring blue cell in an entosis-like process. Maître et al. (2015) showed that cells internalize only  
 514 when differences in surface contractility exceed a predictable threshold, in particular, when tension asym-  
 515 metry  $\delta := \sigma_{BM}/\sigma_{RM} \geq 1 + 2\alpha$  where compaction parameter  $\alpha := \sigma_{BR}/2\sigma_{RM}$ . This translates to a cell  
 516 internalization condition  $\sigma_{BM} \geq \sigma_{RM} + \sigma_{BR}$ . Consider an initial configuration of a cell doublet on a cubical  
 517 domain  $\Omega = [0, 1] \times [0, 1] \times [0, 1]$  discretized uniformly into  $m = 100 \times 100 \times 100$  points. We present a  
 518 three-dimensional numerical simulation using our level set-based scheme with time step size  $\delta t = 0.0015$  and

519 interfacial tensions  $\sigma_{BM} = 2.05$ , and  $\sigma_{RM} = \sigma_{BR} = 1.0$  satisfying the cell internalization condition (see  
520 Figure 13 and Movie S11). This confirms that our method produces similar results as in (Maître et al.,  
521 2015), and more importantly, it can handle simulations in higher dimensions.

## 522 8. Conclusion

523 In this article, we have presented in detail a mathematical model for cellular rearrangements occurring  
524 in tissue morphogenesis. This model is based on free energy minimization and in this sense, it is not  
525 new. The novel part of the model lies in the way how cellular shapes are mathematically represented and  
526 how the equations are numerically solved. To be precise, we adopt an implicit representation of cellular  
527 junctions based on the Osher-Sethian level set method and find their evolution numerically by employing  
528 a thresholding scheme, which features good compatibility with the level set representation and a solid  
529 mathematical background including stability and convergence.

530 We have augmented the model with several aspects pertinent to cell biology, most importantly, a localiza-  
531 tion step which prevents cells from unnatural splitting during their rearrangement. The resulting numerical  
532 model has four major advantages: (1) it is able to express curved shapes of cell-cell junctions which is in-  
533 dispensable for finding the correct energy minimum; (2) it implicitly realizes the correct cell contact angles;  
534 (3) it has minimal number of parameters which is essential in using the model as a tool for testing biological  
535 hypotheses; and (4) it correctly handles cell intercalations and other topology changes, which follows from  
536 the mathematical theory. We have shown that in this respect, the proposed computational model surpasses  
537 other commonly used computational models, such as vertex dynamics model, cellular Potts model, and finite  
538 element-based method. The cost of having these advantages is that the mathematical representation is less  
539 intuitive than the explicit approaches, as that of the vertex dynamics or finite elements, and that it may  
540 require more of computational time than the classical methods. However, the comparison of computational  
541 times depends on the problem solved, as explained in Section 4.

542 In order to express certain morphological phenomena, it may be necessary to extend the model, e.g., to  
543 deal with situations where the dynamics is not only relevant around cell-cell junctions, but also in the inner  
544 region; or situations where the surface tension varies with respect to the position on the cell-cell junction.  
545 These extensions will be addressed in our forthcoming work.

546 Nevertheless, we have shown on several specific examples that the proposed model is applicable to a wide  
547 range of morphological phenomena which includes the range of all commonly used models, starting with the  
548 classical cell sorting and blastomere internalization. Most importantly, thanks to the new computational  
549 approach, we have for the first time succeeded in the replication of the complex process of cellular pattern  
550 formation in sensory epithelia.

551 **Acknowledgements**

552 This work was supported by the Japan Society for the Promotion of Sciences through its Grants-in-Aid  
553 for Scientific Research (KAKENHI) [Grant Numbers 19K03634, 19H04965, 18H04764, 18K06219, 17K05368,  
554 18H01139] and Grant-in-aid for JSPS Fellows [Grant Number 18F18016]; and the Japan Science and Tech-  
555 nology Agency through its PRESTO (Precursory Research for Embryonic Science and Technology) Program  
556 [Grant Number JPMJPR1946]. The authors also thank to Mr. Adrien Rey for his cooperation on the  
557 development of the numerical code during his short-term exchange student stay at Kyoto University in 2018.

558 **Data availability statement**

559 All data generated or analyzed during this study are included in this published article (and its supple-  
560 mentary information files) or are fully accessible in the cited previous work.  
561 Accession numbers for cDNAs are listed as below: mouse nectin-1 gene, AF297665.1; mouse nectin-3 gene,  
562 NM\_021495.4; mouse cadherin-1 gene, NM\_009864.3; mouse cadherin-2 gene, NM\_007664.5.

563 **Code availability**

564 All codes used to obtain the simulation data presented in this article are fully available on Code Ocean.

565 **Conflict of interests**

566 We state that we are not aware of any potential conflicts of interest related to this work.

567 **References**

- 568 Armstrong, N.J., Painter, K.J., Sherratt, J.A., 2006. A continuum approach to modelling cell-cell adhesion  
569 243, 98–113.
- 570 Brodland, G.W., 2002. The differential interfacial tension hypothesis (dith): A comprehensive theory for  
571 the self-rearrangement of embryonic cells and tissues. *Journal of Biomechanical Engineering* 124, 188–197.  
572 doi:10.1115/1.1449491.
- 573 Brodland, G.W., 2004. Computational modeling of cell sorting, tissue engulfment, and related phenomena:  
574 A review. *Applied Mechanics Reviews* 57, 47–76. doi:10.1115/1.1583758.
- 575 Brodland, G.W., Chen, H.H., 2000. The mechanics of heterotypic cell aggregates: Insights from computer  
576 simulations. *Journal of Biomechanical Engineering* 122, 402–407. doi:10.1115/1.1288205.
- 577 Brodland, G.W., Gordon, R., 1994. Finite element methods for developmental biology, in: *International*  
578 *Review of Cytology*. Academic Press. volume 150, pp. 95–118. doi:10.1016/S0074-7696(08)61538-7.

- 579 Brodland, G.W., Veldhuis, J.H., 2002. Computer simulations of mitosis and interdependencies between mitosis orientation, cell shape and epithelia reshaping. *Journal of Biomechanics* 35, 673–681. doi:10.1016/S0021-580 9290(02)00006-4.
- 582 Bronsard, L., Wetton, B.T.R., 1995. A numerical method for tracking curve networks moving with curvature motion. *Journal of Computational Physics* 120, 66–87. doi:10.1006/jcph.1995.1149.
- 584 Carrillo, J.A., Murakawa, H., Sato, M., Togashi, H., Trush, O., 2019. A population dynamics model of cell-cell adhesion incorporating population pressure and density saturation. *Journal of Theoretical Biology* 585 474, 14–24. doi:10.1016/j.jtbi.2019.04.023.
- 587 Chen, H.H., Brodland, G.W., 2000. Cell-level finite element studies of viscous cells in planar aggregates. *Journal of Biomechanical Engineering* 122, 394–401. doi:10.1115/1.1286563.
- 589 Dickinson, D.J., Nelson, W.J., Weis, W.I., 2011. A polarized epithelium organized by  $\beta$ - and  $\alpha$ -catenin predates cadherin and metazoan origins. *Science* 331, 1336–1339. doi:10.1126/science.1199633.
- 591 Esedoğlu, S., Otto, F., 2015. Threshold dynamics for networks with arbitrary surface tensions. *Communications on Pure and Applied Mathematics* 68, 808–864. doi:10.1002/cpa.21527.
- 593 Fletcher, A.G., Osborne, J.M., Maini, P.K., Gavaghan, D.J., 2013. Implementing vertex dynamics models of cell populations in biology within a consistent computational framework. *Progress in Biophysics and Molecular Biology* 113, 299–326. doi:10.1016/j.pbiomolbio.2013.09.003.
- 596 Foty, R.A., Steinberg, M.S., 2005. The differential adhesion hypothesis: a direct evaluation. *Developmental Biology* 278, 255–263. doi:10.1016/j.ydbio.2004.11.012.
- 598 Glazier, J.A., Graner, F., 1993. Simulation of the differential adhesion driven rearrangement of biological cells. *Phys. Rev. E* 47, 2128–2154. doi:10.1103/PhysRevE.47.2128.
- 600 Graner, F., Glazier, J.A., 1992. Simulation of biological cell sorting using a two-dimensional extended potts model. *Phys. Rev. Lett.* 69, 2013–2016. doi:10.1103/PhysRevLett.69.2013.
- 602 Harris, A.K., 1976. Is cell sorting caused by differences in the work of intercellular adhesion? a critique of the steinberg hypothesis. *Journal of Theoretical Biology* 61, 267–285. doi:10.1016/0022-5193(76)90019-9.
- 604 Heisenberg, C.P., Bellaïche, Y., 2013. Forces in tissue morphogenesis and patterning. *Cell* 153, 948–962. doi:10.1016/j.cell.2013.05.008.
- 606 Herring, C., 1999. Surface tension as a motivation for sintering, in: Ball, J.M., Kinderlehrer, D., Podio-Guidugli, P., Slemrod, M. (Eds.), *Fundamental Contributions to the Continuum Theory of Evolving Phase Interfaces in Solids: A Collection of Reprints of 14 Seminal Papers*. Springer Berlin Heidelberg, Berlin, Heidelberg, pp. 33–69. doi:10.1007/978-3-642-59938-5\_2.

610 Honda, H., 1983. Geometrical models for cells in tissues, in: Bourne, G.H., Danielli, J.F., Jeon, K.W.  
611 (Eds.), *International Review of Cytology*. Academic Press. volume 81, pp. 191–248. doi:10.1016/S0074-  
612 7696(08)62339-6.

613 Honda, H., Tanemura, M., Nagai, T., 2004. A three-dimensional vertex dynamics cell model of space-  
614 filling polyhedra simulating cell behavior in a cell aggregate. *Journal of Theoretical Biology* 226, 439–453.  
615 doi:10.1016/j.jtbi.2003.10.001.

616 Jacobs, M., Merkurjev, E., Esedoglu, S., 2018. Auction dynamics: A volume constrained mbo scheme. *J.*  
617 *Comput. Physics* 354, 288–310. doi:10.1016/j.jcp.2017.10.036.

618 Katsunuma, S., Honda, H., Shinoda, T., Ishimoto, Y., Miyata, T., Kiyonari, H., Abe, T., Nibu, K.I., Takai,  
619 Y., Togashi, H., 2016. Synergistic action of nectins and cadherins generates the mosaic cellular pattern of  
620 the olfactory epithelium. *The Journal of cell biology* 212, 561–575. doi:10.1083/jcb.201509020.

621 Laux, T., Otto, F., 2016. Convergence of the thresholding scheme for multi-phase mean-curvature flow.  
622 *Calculus of Variations and Partial Differential Equations* 55, 129. doi:10.1007/s00526-016-1053-0.

623 Laux, T., Swartz, D., 2017. Convergence of thresholding schemes incorporating bulk effects. *Interfaces and*  
624 *Free Boundaries* 19, 273–304. doi:10.4171/IFB/383.

625 Maître, J.L., Heisenberg, C.P., 2011. The role of adhesion energy in controlling cell–cell contacts. *Current*  
626 *Opinion in Cell Biology* 23, 508–514. doi:10.1016/j.ceb.2011.07.004.

627 Maître, J.L., Niwayama, R., Turlier, H., Nédélec, F., Hiiragi, T., 2015. Pulsatile cell-autonomous contractility  
628 drives compaction in the mouse embryo. *Nature Cell Biology* 17, 849–855. doi:10.1038/ncb3185.

629 Merriman, B., Bence, J.K., Osher, S.J., 1994. Motion of multiple junctions: A level set approach. *Journal*  
630 *of Computational Physics* 112, 334–363. doi:10.1006/jcph.1994.1105.

631 Misiats, O., Yip, N., 2016. Convergence of space-time discrete threshold dynamics to anisotropic motion by  
632 mean curvature. *Discrete and Continuous Dynamical Systems - A* 36, 6379–6411.

633 Morgan, F., 1997. Lowersemicontinuity of energy clusters. *Proceedings of the Royal Society of Edinburgh:*  
634 *Section A Mathematics* 127, 819–822. doi:10.1017/S0308210500023842.

635 Mullins, W.W., 1999. Two-dimensional motion of idealized grain boundaries, in: Ball, J.M., Kinderlehrer,  
636 D., Podio-Guidugli, P., Slemrod, M. (Eds.), *Fundamental Contributions to the Continuum Theory of*  
637 *Evolving Phase Interfaces in Solids: A Collection of Reprints of 14 Seminal Papers*. Springer Berlin  
638 Heidelberg, Berlin, Heidelberg, pp. 70–74. doi:10.1007/978-3-642-59938-5\_3.

639 Nagai, T., Honda, H., 2001. A dynamic cell model for the formation of epithelial tissues. *Philosophical*  
640 *Magazine B* 81, 699–719. doi:10.1080/13642810108205772.

- 641 Nose, A., Nagafuchi, A., Takeichi, M., 1988. Expressed recombinant cadherins mediate cell sorting in model  
642 systems. *Cell* 54, 993–1001. doi:10.1016/0092-8674(88)90114-6.
- 643 Osher, S., Sethian, J.A., 1988. Fronts propagating with curvature-dependent speed: Algorithms based  
644 on hamilton-jacobi formulations. *Journal of Computational Physics* 79, 12–49. doi:10.1016/0021-  
645 9991(88)90002-2.
- 646 Salvador, T., Esedoğlu, S., 2019. A simplified threshold dynamics algorithm for isotropic surface energies.  
647 *Journal of Scientific Computing* 79, 648–669. doi:10.1007/s10915-018-0866-8.
- 648 Steinberg, M.S., 1963. Reconstruction of tissues by dissociated cells. *Science* 141, 401–408.  
649 doi:10.1126/science.141.3579.401.
- 650 Steinberg, M.S., Takeichi, M., 1994. Experimental specification of cell sorting, tissue spreading, and specific  
651 spatial patterning by quantitative differences in cadherin expression. *Proceedings of the National Academy  
652 of Sciences of the United States of America* 91, 206–209. doi:10.1073/pnas.91.1.206.
- 653 Takeichi, M., 2014. Dynamic contacts: rearranging adherens junctions to drive epithelial remodelling. *Nature  
654 Reviews Molecular Cell Biology* 15, 397–410. doi:10.1038/nrm3802.
- 655 Togashi, H., 2016. Differential and cooperative cell adhesion regulates cellular pattern in sensory epithelia.  
656 *Frontiers in cell and developmental biology* 4:104. doi:10.3389/fcell.2016.00104.
- 657 Togashi, H., Katsunuma, S., 2017. Cellular recognition and patterning in sensory systems. *Experimental  
658 Cell Research* 358, 52–57. doi:10.1016/j.yexcr.2017.04.005.
- 659 Togashi, H., Kominami, K., Waseda, M., Komura, H., Miyoshi, J., Takeichi, M., Takai, Y., 2011. Nectins  
660 establish a checkerboard-like cellular pattern in the auditory epithelium. *Science* 333, 1144–1147.  
661 doi:10.1126/science.1208467.
- 662 Xu, X., Wang, D., Wang, X.P., 2017. An efficient threshold dynamics method for wetting on rough surfaces.  
663 *Journal of Computational Physics* 330, 510–528. doi:10.1016/j.jcp.2016.11.008.

## 664 **Appendix A. Energy Approximation, Relaxation, and Linearization**

665 Following the lines in (Esedoğlu and Otto, 2015), we briefly explain the derivation of the algorithm for  
666 the gradient descent minimization of the energy

$$E(\mathcal{C}_1, \dots, \mathcal{C}_N) = \sum_{i \neq j} \sigma_{ij} \text{Area}(\gamma_{ij}) \quad (\text{A.1})$$

667 under the volume constraints

$$\text{Volume}(\mathcal{C}_j) = V_j^0, \quad j = 1, \dots, N. \quad (\text{A.2})$$

668 The area (corresponds to "length" in a two-dimensional model) of a cell-cell junction  $\gamma_{ij}$  can be estimated  
 669 using the so-called "heat content approximation", which says that the area of the junction is proportional  
 670 to the heat that flows from cell  $\mathcal{C}_j$  to cell  $\mathcal{C}_i$  in a short time  $\delta t$ :

$$\text{Area}(\gamma_{ij}) \approx \frac{1}{\sqrt{\delta t}} \int \chi_{\mathcal{C}_i} G_{\delta t} * \chi_{\mathcal{C}_j} dx. \quad (\text{A.3})$$

671 Here  $G_{\delta t}(x) = (4\pi\delta t)^{-\frac{d}{2}} e^{-\frac{|x|^2}{4\delta t}}$  is the  $d$ -dimensional Gaussian kernel,  $d$  is the spatial dimension of the model,  
 672 and  $\chi_{\mathcal{C}}$  denotes the characteristic function of a cell region  $\mathcal{C}$ . Hence, multiplying by the weights  $\sigma_{ij}$  and  
 673 adding over all junctions, the energy  $E$  can, with a small error, be replaced by

$$E(\mathcal{C}_1, \dots, \mathcal{C}_N) \approx E_{\delta t}(\mathbf{u}) := \frac{1}{\sqrt{\delta t}} \sum_{i,j=1}^N \sigma_{ij} \int u_i G_{\delta t} * u_j dx, \quad (\text{A.4})$$

674 where we have expressed the cell regions  $\mathcal{C}_k, k = 1, \dots, N$  by a vector-valued function  $\mathbf{u} = (u_1, \dots, u_N)$  on  
 675  $\Omega$ , whose components  $u_k(x)$  can take only two values: 1 if the point  $x$  belongs to  $\mathcal{C}_k$ , or 0 if it does not. It  
 676 was shown that  $E_{\delta t}$  is a correct approximation of the original energy  $E$  in the sense that it  $\Gamma$ -converges to  
 677  $E$  when  $\delta t \rightarrow 0$ .

678 Due to the condition on the cell volumes, the function  $\mathbf{u}$  is constrained to belong to the set

$$\mathcal{B} := \left\{ \mathbf{u} \in \{0, 1\}^N : \sum_{j=1}^N u_j(x) = 1, \text{ a.e. } x \in \Omega \text{ and } \int_{\Omega} u_j = V_j^0, j = 1, \dots, N \right\}, \quad (\text{A.5})$$

where  $\Omega$  is the domain occupied by the cells. This set is not convex, which poses a difficulty in the mini-  
 mization problem, but it can be shown in a similar fashion to (Esedoglu and Otto, 2015) that the minimum  
 of  $E_{\delta t}$  over  $\mathcal{B}$  coincides with the minimum over the convex set  $\mathcal{K}$  obtained from  $\mathcal{B}$  by relaxation, i.e., by  
 allowing the components of  $\mathbf{u}$  to take any value between 0 and 1:

$$\mathcal{K} := \left\{ \mathbf{u} \in [0, 1]^N : \sum_{j=1}^N u_j(x) = 1, \text{ a.e. } x \in \Omega \text{ and } \int_{\Omega} u_j = V_j^0, j = 1, \dots, N \right\}.$$

679 The approximate energy  $E_{\delta t}$  is still nonlinear, so to devise a simple minimization scheme, we adopt  
 680 the approach of iterative minimization, which is justified by Lemma 5.2 of (Esedoglu and Otto, 2015).  
 681 Namely, we assume that we have an approximation of the minimizer  $\mathbf{u}^k$  of  $E_{\delta t}$  in  $\mathcal{K}$  and compute a updated  
 682 approximation  $\mathbf{u}^{k+1}$  by linearizing the energy  $E_{\delta t}(\mathbf{u})$  around  $\mathbf{u}^k$  and defining  $\mathbf{u}^{k+1}$  to be the minimizer of  
 683 the linearized energy over  $\mathcal{K}$ :

$$\mathbf{u}^{k+1} = \arg \min_{\mathbf{u} \in \mathcal{K}} \mathcal{L}_{E_{\delta t}}(\mathbf{u}; \mathbf{u}^k). \quad (\text{A.6})$$

684 Here  $\mathcal{L}_{E_{\delta t}}$  is the linearized energy given by

$$\mathcal{L}_{E_{\delta t}}(\mathbf{u}; \mathbf{u}^k) = \frac{2}{\sqrt{\delta t}} \sum_{i=1}^N \int u_i \varphi_i^k dx, \quad \varphi_i^k := \sum_{j=1}^N \sigma_{ij} G_{\delta t} * \mathbf{u}^k. \quad (\text{A.7})$$

685 The functions  $\varphi_i^k$  correspond to the functions  $\psi_i^k$  in the main algorithm. It was proved in (Esedoglu and Otto,  
 686 2015) and (Laux and Otto, 2016) that in the absence of volume constraints the sequence  $\{\mathbf{u}^k\}$  decreases the

687 approximate energy  $E_{\delta t}$  in every step and correctly approximates the  $L^2$ -gradient flow of the original energy  
 688  $E$  in the limit  $\delta t \rightarrow 0$ .

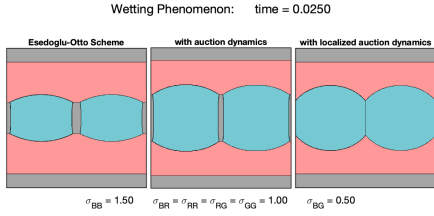
689 In the case when there is no volume constraint, the minimization problem (A.6) becomes a problem of  
 690 minimizing a linear function over a simplex set  $\mathcal{K}$  and thus the solution is obtained immediately as

$$u_i^{k+1}(x) = \begin{cases} 1 & \text{if } \varphi_i^k(x) = \min_j \varphi_j^k(x) \\ 0 & \text{otherwise .} \end{cases} \quad (\text{A.8})$$

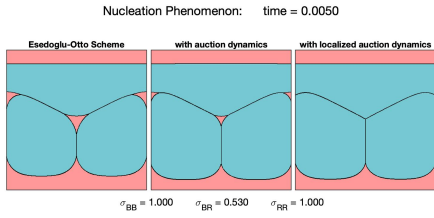
691 This leads to a very simple thresholding scheme. However, when the set  $\mathcal{K}$  includes volume constraints, the  
 692 solution of the minimization (A.6) involves unknown Lagrange multipliers  $\lambda_{ij}$ :

$$u_i^{k+1}(x) = \begin{cases} 1 & \text{if } \varphi_i^k(x) = \min_j (\varphi_j^k(x) + \lambda_{ij}) \\ 0 & \text{otherwise .} \end{cases} \quad (\text{A.9})$$

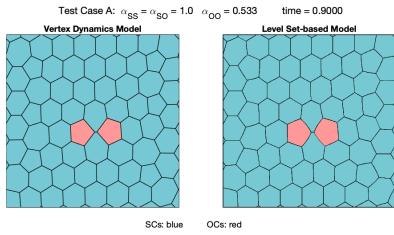
693 Direct computation of the Lagrange multipliers for more than 3 cells is complicated and can be avoided by  
 694 the application of auction algorithm, as explained in Section 2.



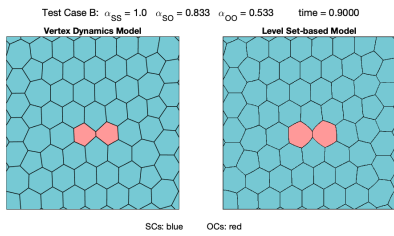
Movie S1: Wetting phenomenon in the numerical implementation of level set-based methods. Initial 4-cell configuration and its evolution under a wetting condition due to violation of  $\sigma$ -triangle inequality at  $t = 50\delta t$  using Esedoglu-Otto scheme only (left); EO scheme with auction dynamics algorithm (center); and EO scheme with localized auction dynamics (right).



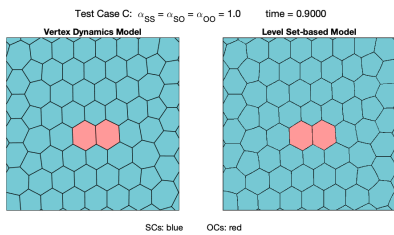
Movie S2: Nucleation phenomenon in the numerical implementation of level set-based methods. Initial 4-cell configuration and its evolution at  $t = 10\delta t$  using Esedoglu-Otto algorithm (left) resulting in nucleation of red cell at the blue triple junction; EO scheme with auction dynamics (center) where red cell splitting persists; and EO scheme with localized auction dynamics (right) which preserves cell connectivity.



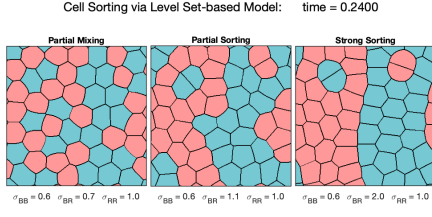
Movie S3: Vertex dynamics vs. Level set-based model on Test Case A, where adhesion strengths are  $\alpha_{SS} = \alpha_{SO} = 1.0$  and  $\alpha_{OO} = 0.533$  leading to cellular intercalation. Initial aggregate of 62 SCs (blue) and 2 OCs (red), and its evolution via vertex dynamics model with volume penalty  $\rho = 500$  (left) and level set-based approach (right).



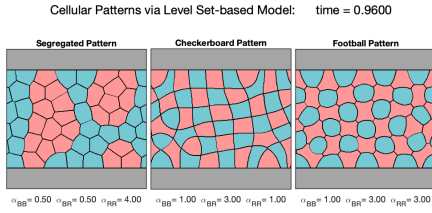
Movie S4: Vertex dynamics vs. Level set-based model on Test Case B, where adhesion strengths are  $\alpha_{SS} = 1.0$ ,  $\alpha_{SO} = 0.833$  and  $\alpha_{OO} = 0.533$  where no intercalation occurs. Initial aggregate of 62 SCs (blue) and 2 OCs (red), and its evolution via vertex dynamics model with volume penalty  $\rho = 500$  (left) and level set-based approach (right).



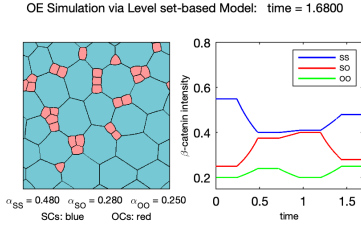
Movie S5: Vertex dynamics vs. Level set-based model on Test Case C, where adhesion strengths are  $\alpha_{SS} = \alpha_{SO} = \alpha_{OO} = 1.0$  which shortens OO-junction. Initial aggregate of 62 SCs (blue) and 2 OCs (red), and its evolution via vertex dynamics model with volume penalty  $\rho = 500$  (left) and level set-based approach (right).



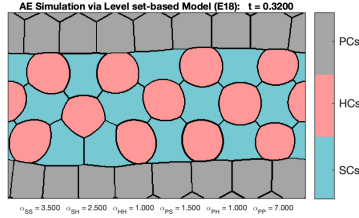
Movie S6: Cell sorting via level set-based model. Initial aggregate of 25 blue and 25 red cells with interfacial tensions  $\sigma_{BB} = 0.6$  and  $\sigma_{RR} = 1.0$ ; its evolution generated by the level set-based approach for partial mixing when  $\sigma_{BR} = 0.7$  (left); partial sorting when  $\sigma_{BR} = 1.1$  (center); and strong sorting when  $\sigma_{BR} = 2.0$  (right).



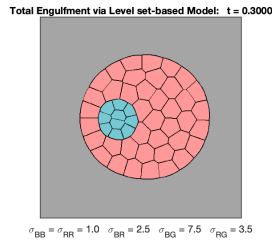
Movie S7: Cellular patterns via level set-based model according to hypothetical profiles of synergistic actions of nectins and cadherins. Initial 48-cell aggregate consisting of 24 blue cells expressing nectin-2 and N-cadherin; and its evolution via level set-based approach resulting in different mosaic patterns: a segregated pattern (left) with red cells expressing nectin-2, N-cadherin, and E-cadherin; a checkerboard pattern (center) with red cells expressing nectin-3 and N-cadherin; and football (right) pattern with red cells expressing nectin-3, N-cadherin, and E-cadherin.



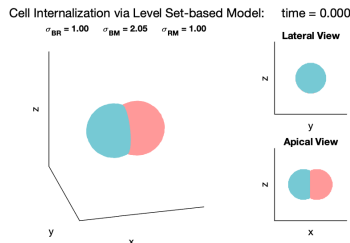
Movie S8: Simulation of a developing olfactory epithelium via level set-based model. Cellular rearrangement of an olfactory epithelium from initial configuration to embryonic stages E14, E16, E18 until postnatal P1 stage generated via our level set-based model using cell-cell adhesion strengths based on  $\beta$ -catenin measurements in Katsunuma et al. (2016).



Movie S9: Simulation of a developing auditory epithelium via level set-based model. Cellular rearrangement of an embryonic auditory epithelium from embryonic stage E14 to E18 generated via our level set-based model.



Movie S10: Total engulfment via level set-based model. An initial aggregate of 10 blue and 40 red cells surrounded by a medium and its evolution generated by our level set-based model; resulting in the total engulfment of the blue cell mass by the red cell mass where interfacial tensions are  $\sigma_{BB} = \sigma_{RR} = 1.0$ ,  $\sigma_{BM} = 7.5$ ,  $\sigma_{RM} = 3.5$ , and  $\sigma_{BR}$  linearly changing from 7.5 (at  $t = 0$ ) to 2.5 (at  $t = 100\delta t$ ) and then kept constant.



Movie S11: Cell internalization via level set-based model. An initial 3D cell doublet configuration (left) and its evolution using our level set-based approach, having interfacial tensions  $\sigma_{BM} = 2.05$ , and  $\sigma_{RM} = \sigma_{BR} = 1.0$ ; and their corresponding lateral view (top right) and apical view (bottom right).